

# Progenitors of low-mass binary black-hole mergers in the isolated binary evolution scenario

Federico García<sup>1</sup>, Adolfo Simaz Bunzel<sup>2</sup> <sup>★</sup>, Sylvain Chaty<sup>1,3</sup>, Edward Porter<sup>3</sup>, and Eric Chassande-Mottin<sup>3</sup>

<sup>1</sup> AIM, CEA, CNRS, Université Paris-Saclay, Université de Paris, F-91191 Gif-sur-Yvette France

<sup>2</sup> Instituto Argentino de Radioastronomía, Universidad Nacional de La Plata, 1900 La Plata, Argentina

<sup>3</sup> Université de Paris, CNRS, Astroparticule et Cosmologie, F-75013 Paris France

received ... 2020 ; accepted ... 2020

## ABSTRACT

**Context.** The formation history, progenitor properties and expected rates of the binary black holes discovered by the LIGO-Virgo collaboration, through the gravitational-wave emission during their coalescence, are now a topic of active research.

**Aims.** We aim to study the progenitor properties and expected rates of the two lowest-mass binary black hole mergers, GW 151226 and GW 170608, detected within the first two Advanced LIGO-Virgo observing runs, in the context of the classical isolated binary-evolution scenario.

**Methods.** We use the publicly-available 1D-hydrodynamic stellar-evolution code MESA, which we adapted to include the black-hole formation and the unstable mass transfer developed during the so-called common-envelope phase. Using more than 50 000 binary simulations, we explore a wide parameter space for initial stellar masses, separations, metallicities and mass-transfer efficiencies. We obtain the expected distributions for the chirp mass, mass ratio and merger time delay by accounting for the initial stellar binary distributions. We predict the expected merger rates that we compare with the detected gravitational-wave events, and study the dependence of our predictions with respect to (yet) unconstrained parameters inherent to binary stellar evolution.

**Results.** Our simulations for both events show that, while the progenitors we obtain are compatible over the entire range of explored metallicities, they show a strong dependence on the initial masses of the stars, according to stellar winds. All the progenitors found follow a similar evolutionary path, starting from binaries with initial separations in the  $30 - 200 R_{\odot}$  range, experiencing a stable mass transfer interaction before the formation of the first black hole, and a second unstable mass-transfer episode leading to a common-envelope ejection that occurs when the secondary star crosses the Hertzsprung gap. The common-envelope phase plays a fundamental role in the considered low-mass range: only progenitors experiencing such an unstable mass-transfer phase are able to merge in less than a Hubble time.

**Conclusions.** We find that all the integrated merger rate densities are below  $\lesssim 0.5 \text{ yr}^{-1} \text{ Gpc}^{-3}$  in the local Universe, the highest rate density being compatible with the observed rates. The common-envelope efficiency  $\alpha_{\text{CE}}$  has a strong impact on the progenitor populations. A high-efficiency scenario with  $\alpha_{\text{CE}} = 2.0$  is favoured when comparing the expected rates with observations.

**Key words.** gravitational waves – binaries:close – stars: evolution – stars: black holes

## 1. Introduction

In 2015, the Advanced LIGO and Advanced Virgo collaboration (LVC) began a series of observation runs. During both the O1 (September 12, 2015 - January 19, 2016) and O2 (November 30, 2016 - August 25, 2017) observation runs, a total of 11 gravitational wave (GW) events were observed. Ten of these events were the detection of signals from the merger of binary black holes (BBHs, Abbott et al. 2019a) and one corresponded to the merger of two neutron stars (Abbott et al. 2017a, GW170817).

While these BBH are mainly dominated by high-mass components ( $M \gtrsim 35 M_{\odot}$ ), two detections in particular, GW151226 (Abbott et al. 2016) and GW170608 (Abbott et al. 2017b), are low-mass systems having BH masses consistent with those found in X-ray binaries (i.e.  $M \lesssim 20 M_{\odot}$ ). Despite that all these events could belong to the same population (Abbott et al. 2019b), the existence and abundance of these objects trigger the question of their formation history. Several scenarios have been proposed in the literature, including the isolated binary evolution (our main focus here, Tauris et al. 2017), dynamical formation (Bae

et al. 2014; Rodriguez et al. 2016) and chemically-homogeneous evolutionary channels (Marchant et al. 2016).

In the dynamical formation scenario, BBHs are produced by three-body encounters in stellar clusters. In the chemically homogeneous evolutionary channel, compact BBHs are formed from rapidly rotating stars in near contact binaries that experience efficient internal mixing. It is estimated that the former contributed to less than a few percent of all observed events (Bae et al. 2014; Rodriguez et al. 2016); while the latter is not able to produce BBH in low-mass range, with  $M \lesssim 10 M_{\odot}$  (Marchant et al. 2016). In this study, we concentrate on the classical isolated binary evolution scenario where the formation of the ultracompact binary leading to the BBH merger is driven through an unstable mass-transfer phase where a common-envelope (CE) is ejected (Ivanova et al. 2013; Kruckow et al. 2016).

Our main goal is to study the progenitor population of the lightest BBHs detected by Advanced LIGO and Advanced Virgo during their first two science runs, O1 and O2, and its dependence on the uncertainties intrinsically related to binary stellar evolution such as the accretion efficiency during a stable mass-transfer phase, efficiency of the CE ejection, impact of metallicity and the evolution of merger rates with redshift.

<sup>★</sup> Fellow of CONICET

This kind of studies has been usually performed following a binary population synthesis approach using several different numerical codes (Lipunov et al. 1997; Belczynski et al. 2002; Voss & Tauris 2003; Belczynski et al. 2016; Eldridge & Stanway 2016; Stevenson et al. 2017; Kruckow et al. 2018; Spera et al. 2019). In this work, we perform detailed numerical stellar simulations of the binary systems, using the 1D-hydrodynamic stellar-evolution code **MESA**. Such kind of treatment, which has been recently growing (see, for instance, Marchant et al. 2017), allows for an accurate modelling of the mass-transfer between the binary components, that has consequences on the final BH masses before the merger. However, the method is computationally expensive, which is the reason why it is usually not considered in standard binary population studies. Our simulations incorporate the evolution during the CE phase, which plays a fundamental role in the considered low-mass BBH range.

The paper is organised as follows: we first describe the binary stellar evolution using **MESA** in Section 2, we then focus on the results for GW 170608 and GW 151226 in Section 3, before reporting on the population-weighted results in Section 4, and giving the projected merger and gravitational-wave event rates in Section 5. We finally discuss the results in Section 6, and summarise and conclude this paper in Section 7.

## 2. Binary stellar evolution using **MESA**

Here, we present models of stellar-binary systems that evolve starting from zero-age main sequence (ZAMS), through to the formation of binary black holes (BBH) and their final merger through the emission of gravitational waves (GW). We made use of the publicly-available stellar evolution code, **MESA** (Paxton et al. 2019, 2018, 2013, 2011, 2010), which we modified to include a treatment for the common-envelope (CE) phase, BH formation, and to properly merge in a single run the three evolutionary stages involved in this problem, that is: a binary of massive stars, massive stellar evolution and BH formation, and the formation of a binary BH.

### 2.1. Microphysics, nuclear networks and stellar winds

Our simulations of non-rotating binaries are computed using **MESA** version 10398. We use CO-enhanced opacity tables from the OPAL project (Iglesias & Rogers 1993, 1996). Convection is modelled following the standard mixing-length theory (MLT, Böhm-Vitense 1958) adopting a mixing-length parameter  $\alpha_{\text{MLT}} = 1.5$ . Convective regions are determined using the Ledoux criterion. In late evolutionary stages of massive stars, the convective velocities in certain regions of the convective envelope can approach the speed of sound, running out of the domain of applicability of the MLT. For these regions, we use an MLT++ treatment (Paxton et al. 2013) that reduces the superadiabaticity. Semi-convection is included according to the diffusive approach presented in Langer et al. (1983) which depends on an efficiency parameter that we assume to be  $\alpha_{\text{SC}} = 1.0$ . We also include a convective-core overshooting during H burning extending the core radius given by the Ledoux criterion by 0.335 of the pressure-scale height ( $H_P$ , Brott et al. 2011). When mass is transferred from one star to its companion, the material accreted by the accretor may have a mean molecular weight higher than its outer layers. This leads to an unstable situation that induces a thermohaline mixing (Kippenhahn et al. 1980), which is included by adopting  $\alpha_{\text{th}} = 1.0$ .

We use standard thermonuclear reaction networks provided by **MESA**: **basic.net** for the hydrogen and helium burning

phases, and switch during run time to **co\_burn.net** for the carbon burning phase. Furthermore, stellar winds are modelled using mass loss rates depending on effective temperatures and surface H mass fraction ( $X_s$ ). When  $T_{\text{eff}} > 10^4$  K, for  $X_s \geq 0.4$  we use the prescription from Vink et al. (2001), while for  $X_s < 0.4$  we apply that from Nugis & Lamers (2000). When  $T_{\text{eff}} < 10^4$  K, we adopt the prescription from de Jager et al. (1988).

### 2.2. From stellar binaries to binary black holes

Stellar binaries and their interactions are modelled using the **MESAbinary** module of **MESA**. Our simulations start when both stars with masses  $M_{i,1}$  and  $M_{i,2}$  are at the zero-age main sequence (ZAMS), in circular orbits, at a certain initial separation  $a_i$ .

The simulation includes an accurate description of the exchange of mass between the two binary components. To determine which star is the donor or the accretor, the atmospheric transfer (MT) rates of both stars is compared according to Ritter (1988). When one of the stars overfills its Roche lobe (RLO), we apply an implicit MT scheme to obtain the MT rate ( $\dot{M}_{\text{RLO}}$ ) at each step. The MT stability is controlled as described in Sec. 2.4.

The MT efficiency,  $\epsilon$ , is assumed to remain constant throughout the entire evolution, and only considers the mass lost through an isotropic wind in the vicinity of the accretor. Assuming no mass loss from either direct fast winds, or a circumbinary co-planar toroid, the MT efficiency  $\epsilon = 1 - \beta$  is defined through the  $\beta$  parameter from **MESAbinary**.

Once the first BH is formed in the system, we use the point mass approximation from **MESAbinary** and we limit the accretion onto the compact object to a factor of the Eddington rate  $\dot{M}_{\text{Edd,BH}} = 4\pi GM_{\text{BH}}/\eta\kappa_{\text{donor}}$ , where  $G$  is the gravitational constant,  $\kappa_{\text{donor}}$  is the opacity of the donor star at its surface and  $\eta$  is the radiation efficiency of the BH which we set to 1% implying super-Eddington accretion. The change in the orbital angular momentum is inferred from the effects of mass loss in the binary (MT and stellar winds).

If a second BH forms, thus leading to a BBH, the time to merger,  $t_{\text{merger}}$ , is estimated from Peters (1964) based on the component masses ( $M_{\text{BH}}$ ), their mutual separation and eccentricity.

### 2.3. Black hole formation

When a non-degenerate star completes the carbon core burning phase, its evolution is stopped as the binary parameters will not change appreciably during the later evolutionary stages due to their short duration (Tauris & van den Heuvel 2006). BH formation is modelled assuming an instantaneous, spherically symmetric ejection of the H and He stellar envelopes. We neglect any interaction with the binary companion and do not consider asymmetric kicks. To update the orbital parameters of the binary immediately after BH formation, we follow Bhattacharya & van den Heuvel (1991) and assume that the mass of the BH remnant is 80% of the stellar CO core mass. The remaining 20% accounts for the release of gravitational binding energy.

We check for possible binary disruption, considering the following parameters: the mass ejected, the final separation and eccentricity. While this recipe for BH formation and compact object final mass is clearly not unique, it appears efficient for the modelling of binary evolution. Core-collapse and compact object formation is a highly-debated topic (see, for instance, Fryer et al. 2012; Sukhbold et al. 2016, and references therein). A comparison between our prescription and others present in the literature can be found in Appendix A.

## 2.4. Common-envelope phase

### 2.4.1. Definition

A common-envelope (CE) phase occurs when the MT becomes unstable. The stability of MT in binary systems is usually understood in terms of the reaction of the binary components to mass accretion or loss (Soberman et al. 1997). Binary population synthesis (BPS) codes generally associate the MT stability to the binary mass ratio at the onset of the MT phase. If this ratio is above some limit, then the MT is considered unstable thus, typically, leading to a CE phase.

However, this was recently revised in Pavlovskii & Ivanova (2015) and Pavlovskii et al. (2017), showing that the mass ratio condition is not sufficient, nor necessary, to predict the outcome of the MT phase. In these papers based on numerical stellar evolution, the authors show that binaries with mass ratio  $q = m_2/m_1$  as high as 0.13 experience a stable MT phase, contradicting earlier works (e.g., Belczynski et al. 2008).

Based on these recent works we introduce new conditions for deciding the MT stability using the rate of mass transfer  $\dot{M}_{\text{RLOF}}$  during the RLO at different evolutionary stages. We assume the MT to be unstable when, during RLO, the MT rate exceeds a certain value that we fix to the Eddington limit of the donor,  $M_{\text{Edd}} = 4\pi c R / \kappa$ , where  $R$  is the stellar radius and  $c$  is the speed of light. When the binary consists of two non-degenerate stars, we also consider unstable MT if the MT rate is higher than the Eddington limit of the accretor. In our simulations these MT rates are of the order of  $\sim 10^{-2} M_{\odot} \text{ yr}^{-1}$ , consistent with the value assumed by Quast et al. (2019) for unstable MT. In contrast to population synthesis codes, **MESA** allows us to calculate the MT rate at each evolutionary time step. It is thus possible to continuously verify these conditions, even when the binary experiences a RLO phase. This additionally allows us to detect late phases of unstable MT rates in the case of long and initially stable RLO phases.

When any of the above conditions are met, a so-called CE phase is triggered. During this phase, the donor star engulfs its companion, while the accretor in-spirals inside the envelope of the donor. A successful envelope ejection may occur on a dynamical timescale (Podsiadlowski 2001). It is important to note that the uncertainties associated with this phase are of central importance in the evaluation of predicted rates of GW events, since as mentioned in Section 1, merger time delay of BBHs are strongly dependent on the separation and eccentricity of the BBH just after the second BH has formed. In particular, no BBH is expected to merge in less than the Hubble time when the post-CE system is not ultra-compact in nature. Furthermore, the CE phase plays a crucial role in reducing the separation between two stars, or between a star and a BH, in a binary system, by a factor of 10 to 100 (Tauris et al. 2017).

### 2.4.2. Numerical implementation

In order to implement a numerical treatment for the CE phase within **MESA**, we use the so-called energy formalism (Webbink 1984; de Kool 1990). According to this formalism, the main energy source needed to eject the stellar envelope is provided by the orbital energy reservoir and thus, by the in-spiral of the companion. Changes in these two quantities are related by a free parameter  $\alpha_{\text{CE}}$  representing the fraction of the orbital energy deposited as kinetic energy of the envelope components:

$$\Delta E_{\text{bind}} = \alpha_{\text{CE}} \Delta E_{\text{orb}}, \quad (1)$$

where  $\Delta E_{\text{bind}}$  is the change in the binding energy of the donor star envelope, while  $\Delta E_{\text{orb}}$  represents the released orbital energy throughout the in-spiral, and  $\alpha_{\text{CE}}$  is the CE efficiency that we assume to be fixed throughout the entire CE phase. Here,  $E_{\text{bind}}$  is given by

$$E_{\text{bind}} = \int_{M_{\text{core}}}^M \left( -\frac{Gm_r}{r} + u \right) dm_r \quad (2)$$

which includes both the gravitational binding energy and the specific internal energy of the envelope. The latter has an additional term associated to the recombination energy of available H and He, known to help with the ejection of the envelope (Ivanova et al. 2015; Nandez et al. 2015; Kruckow et al. 2016).

Given an unstable MT rate  $\dot{M}$ , during the time step  $\Delta t$ , the donor losses a mass  $\Delta M = \dot{M}\Delta t$  from its outer layer, changing its envelope binding energy by  $\Delta E_{\text{bind}}$ , and consequently the orbital energy by  $\Delta E_{\text{orb}}$ , which naturally leads to the spiral-in of the binary.

For numerical stability reasons, once a CE phase is triggered, during a fixed amount of time (that we set to 10 yr), we linearly increase the MT rate up to a fixed maximum value (that we set to  $10^{-1} M_{\odot} \text{ yr}^{-1}$  throughout this work), and the mass accretion onto the companion is turned off (Ivanova et al. 2013). Once the maximum value for the MT rate is reached, we keep that value constant until the donor star detaches, i.e., its radius becomes smaller than its corresponding Roche lobe, or until the merger of the two stars becomes unavoidable, i.e., the envelope could not be successfully ejected, leading to a single star or a so-called Thorne-Zytkow object (TZO, Thorne & Zytkow 1977). In this latter case, the evolution is stopped as it would not lead to a BBH<sup>1</sup>. In the former case, when reaching the detach condition, the mass transfer rate  $\dot{M}_{\text{RLOF}}$  is linearly decreased, as a fraction of the radius of the lobe, down to the mass loss  $\dot{M}_{\text{th}}$  obtained at thermal equilibrium. For those surviving binaries, the donor star becomes an almost naked core, with a tiny envelope rich in H, and with a close companion. The evolution then returns to the standard **MESA** workflow, allowing for a new stable RLO phase to start.

## 2.5. MESA runs

As our main goal is to study the progenitor population of the lightest BBHs detected by the LVC during the O1/O2 runs, we explore a wide range of metallicities, i.e.  $Z = 0.001, 0.004, 0.007$  and  $0.015$ , which, in principle, can lead to BHs in the mass range of interest. In addition, in order to study the dependence of our results on the poorly-known MT efficiency, we cover a wide range for this parameter with four different values:  $\epsilon = 0.6, 0.4, 0.2$  and  $0.0$ , going from efficient to fully inefficient regimes. For each pair of  $Z$  and  $\epsilon$  values, we compute a 3D grid in the parameter space formed by the initial masses ( $M_{i,1}, M_{i,2}$ ) and the binary initial separation ( $a_i$ ).

As a first approach, we fix  $\alpha_{\text{CE}} = 2.0$ <sup>2</sup>, and explore a wide range of initial separations, from  $30 - 4000 R_{\odot}$  in logarithmic

<sup>1</sup> We assume that a merger happens in a binary when the reduction in separation leads to a relative donor overflow  $r_{\text{RL}} = \frac{R - R_{\text{RL}}}{R_{\text{RL}}}$  bigger than a limiting value which we set equal to 20. We found that beyond this value the donor radius cannot become smaller than its corresponding Roche lobe. Additionally, we assume a merger occurs when the simulations would not complete due to convergence issues at late times during the CE phase.

<sup>2</sup> We refer the reader to Ivanova et al. (2013) for a complete discussion on values of CE efficiency parameter  $\alpha_{\text{CE}} \geq 1.0$ .

**Table 1.** Number of MESA runs performed for this work

$\epsilon$	$\alpha_{\text{CE}} = 2.0$	$\alpha_{\text{CE}} = 1.0$
0.6	9822	4861
0.4	9602	8703
0.2	9891	4433
0.0	4331	91
Total	33646	18088

steps of 0.03 dex, and a short range of initial masses:  $30 - 34 \text{ M}_\odot$  for the primary star and  $20 - 24 \text{ M}_\odot$  for the companion, both in steps of  $2 \text{ M}_\odot$ , in order to find regions containing solutions, which we call *target regions*. These regions are obtained for systems with  $a_i < 500 \text{ R}_\odot$ , in which binaries went through a CE phase when the first BH was formed. Once the broad parameter space was understood, we focused our searches on this evolutionary channel, but exploring wider ranges of masses and lowering the grid spacing in  $a_i$  to 0.02 dex, for values below  $500 \text{ R}_\odot$ .

As each MESA simulation is computationally expensive, from this point onward, we set up a strategy to concentrate our runs on the regions that lead to BBHs with masses in the range of interest, avoiding the calculation of binary systems leading to too light or too heavy chirp masses, but also systems that did not display strong interaction (high MT rates) and thus led to extremely long merging times. These ranges depend mainly on  $Z$ , but also on  $\epsilon$ . Thus, for each parameter combination, our runs were set up to cover different ranges, in an iterative fashion, until the target regions were finally bounded.

In order to explore the dependence of our results on the CE efficiency, we ran another set of simulations with  $\alpha_{\text{CE}} = 1.0$ . In this case, we only ran those simulations for which we already had found a CE trigger and had chirp masses in the range of interest. Since the density of CE survivals significantly decreases for this efficiency, due to a natural increase in CE mergers, we decided to increase the grid resolution to  $\Delta M = 1 \text{ M}_\odot$  and 0.01 dex in the logarithmic grid of  $a_i$ , and we proceeded to run the 26 first neighbours in the refined grid for each CE survival of the initial runs. After this step we proceeded in an iterative manner surrounding the next family of survivals and so-on until the process converged.

In Table 1 we summarise the 51 734 simulations computed using our MESA-based numerical code for each MT efficiency  $\epsilon$  and CE efficiency  $\alpha_{\text{CE}}$  explored. Full details of the parameter space explored for this work are presented in Appendix B and a full example of a typical MESA simulation leading to a BBH formation after a CE phase is shown in Appendix C.

### 3. Results for GW 151226 and GW 170608

The response of detectors such as Advanced LIGO and Advanced Virgo to a GW compact binary coalescence depends not only on the distance and relative orientation of the GW source to the detector, but also on the intrinsic binary properties; the most important being the chirp mass ( $\mathcal{M}_{\text{chirp}}$ ), which affects the phase evolution of gravitational waveform (Finn 1996) and is defined as,  $\mathcal{M}_{\text{chirp}} = \mu^{3/5} M^{2/5}$  where  $\mu = M_{\text{BH},1} M_{\text{BH},2} / (M_{\text{BH},1} + M_{\text{BH},2})$  is the reduced mass and  $M = M_{\text{BH},1} + M_{\text{BH},2}$  the total mass of the BBH.

GW detections can be used to infer measurements of the redshifted chirp mass in the detector frame, i.e.  $\mathcal{M}_{\text{chirp}}^{\text{detector}} = (1+z)\mathcal{M}_{\text{chirp}}^{\text{source}}$ . In order to estimate  $\mathcal{M}_{\text{chirp}}$  in the source frame, and hence to be able to compare with our theoretical results, the binary masses have to be un-redshifted. Unfortunately, while

a direct measurement of the luminosity distance can be made from an inspiral event, without an electromagnetic counterpart, a cosmological model has to be assumed to extract the redshift of the source. For this work, we used a flat  $\Lambda\text{CDM}$  model with  $H_0 = 70 \text{ km s}^{-1}$  and  $T_{\text{CMB}} = 2.725 \text{ K}$  and the `astropy.cosmology` package (Astropy Collaboration et al. 2013, 2018) to estimate the masses of the lowest-mass BBHs detected by Advanced LIGO-Virgo in O1/O2 runs (Abbott et al. 2019a). We found  $\mathcal{M}_{\text{chirp}} = 8.83_{-0.66}^{+0.74} \text{ M}_\odot$  and  $q_{\text{BBH}} = 0.56_{-0.49}^{+0.44}$  for GW151226 and  $\mathcal{M}_{\text{chirp}} = 7.91_{-0.37}^{+0.43} \text{ M}_\odot$  and  $q_{\text{BBH}} = 0.69_{-0.56}^{+0.31}$  for GW170608, respectively, in their 100% confidence intervals (C.I.).

Throughout this work we consider a certain binary model to be a possible progenitor compatible with any of the GW events under study if its  $\mathcal{M}_{\text{chirp}}$  and  $q_{\text{BBH}}$  lies within the 100% C.I. of the corresponding GW event and if it has a merger time delay ( $t_{\text{merger}}$ ) shorter than the Hubble time ( $\tau_{\text{Hubble}} = 13.46 \text{ Gyr}$ , under our cosmological assumptions).

#### 3.1. Parameter space and target regions

We use models and method described in Sec. 2, in order to find the target region in the 3D parameter space, associated with each GW event, for each metallicity, MT and CE efficiencies.

Figure 1 shows the solution regions for GW151226 and GW170608 obtained with  $\alpha_{\text{CE}} = 2.0$ , along with their merger time delay. In general, more massive progenitors are needed to explain GW151226 than GW170608 in each individual case, in agreement with their final BH masses. Higher metallicities require increasingly massive stars in order to obtain progenitors of both GW events, a direct consequence of the dependence of stellar winds on the metallicity content (see for instance Kudritzki & Puls 2000). We find that this effect is independent of the MT efficiency. For all metallicities explored at the higher MT efficiencies  $\epsilon \geq 0.4$ , we find progenitors compatible with both GW events, while in the more inefficient MT regime, we find that only low metallicity binaries are able to become actual progenitors. This is because at high metallicities and low MT efficiencies, chirp masses found are always below the lower boundaries given by Abbott et al. (2019a) for the least massive BBHs.

Another interesting feature in Figure 1 is that, at low metallicities, when  $Z \leq 0.004$  and high MT efficiencies  $\epsilon \geq 0.4$ , binaries with similar initial masses are admissible progenitors. Efficient accretion favours the growth of a convective core in the accreting star, which in our case is typically located on the main-sequence (MS), leading to a rejuvenation (Braun & Langer 1995; Dray & Tout 2007), and thus a longer duration of the core H-burning phase that can delay the H depletion after the primary (and initially more massive) star collapses to a BH.

However, this behaviour is not observed at high metallicities as rejuvenation is not strong enough to delay H depletion. In this case, after an initial efficient MT phase, the secondary star expands after leaving the MS and both stars overfill their Roche lobes, evolving to an over-contact phase. This, in principle, is not the same as a CE phase as co-rotation can be maintained as long as there is no overflow through the second Lagrangian point (L2) and thus no viscous drag as in the CE phase. Although our simulation does not allow for an over-contact phase, it is expected that BHs produced by this channel have higher masses than the ones found for GW151226 and GW170608 (Marchant et al. 2016). Combining this last line of reasoning with strong winds, we find no solutions for high metallicities and low MT efficiencies.

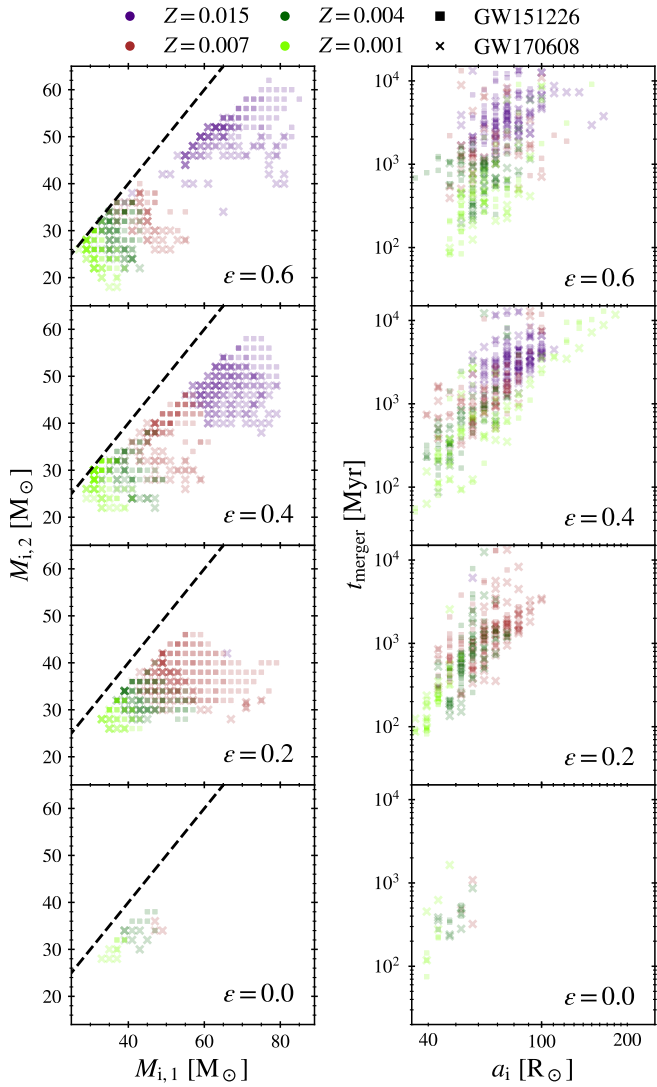
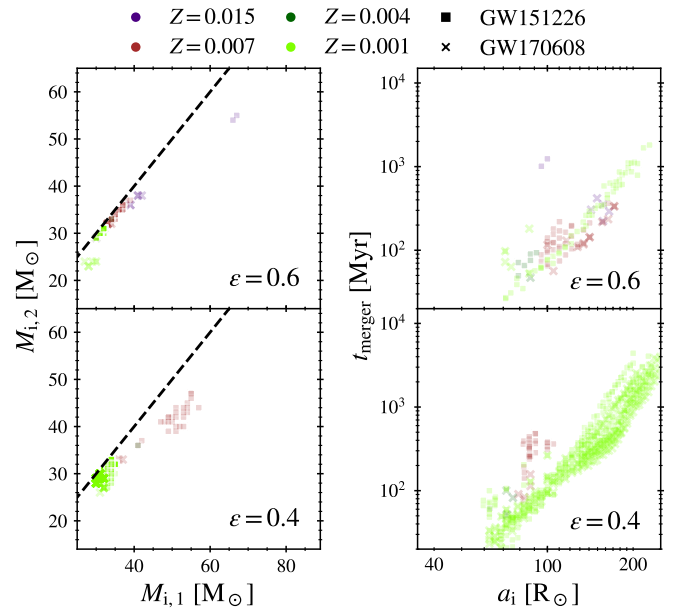


**Fig. 1.** Target regions of the parameter space for GW151226 (square markers) and GW170608 (cross markers) for models with  $\alpha_{\text{CE}} = 2.0$ . On the left panels we show the progenitor initial masses ( $M_{i,1} > M_{i,2}$ ), while on the right panels we plot the merger time delay ( $t_{\text{merger}}$ ) against initial binary separation ( $a_i$ ). Panels from top to bottom correspond to each set of efficiencies:  $\epsilon = 0.6, 0.4, 0.2$  and  $0.0$ . Dashed lines indicate equal progenitor masses.

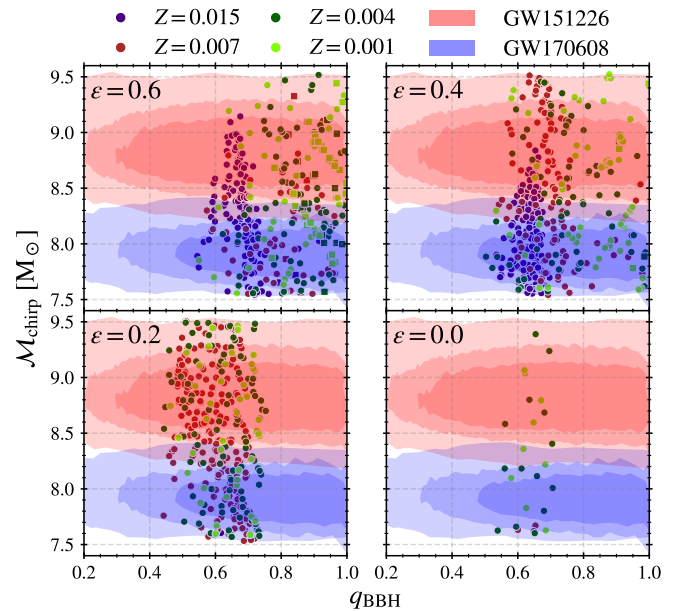
In the right hand side panels of Figure 1, it can be seen that, for all MT efficiencies, increasing  $a_i$  leads to increased merger time delay. In addition, values of  $t_{\text{merger}}$  cover up to two orders of magnitude for a given  $a_i$ . This is explained by the large scatter in mass at BBH formation while separations and eccentricities remain similar after the second BH has formed.

Figure 2 shows the target regions found for  $\alpha_{\text{CE}} = 1.0$ . We see that the progenitors have mass ratios close to unity. The rest of the progenitors obtained with a higher mass ratio either merge during the CE phase or produce BBHs outside the boundaries in  $M_{\text{chirp}}$  and  $q_{\text{BBH}}$ . Independently of the metallicity, no progenitors are found at low MT efficiencies,  $\epsilon \leq 0.2$ .

The solutions obtained for  $\alpha_{\text{CE}} = 2.0$  with  $a_i < 60 R_\odot$  merge during the CE phase when  $\alpha_{\text{CE}} = 1.0$  and thus do not produce BBHs. Additionally, those binaries which end up being compatible progenitors for  $\alpha_{\text{CE}} = 1.0$  have smaller separations at BBH formation than their respective  $\alpha_{\text{CE}} = 2.0$  runs, and thus they all have their associated  $t_{\text{merger}}$  effectively reduced.



**Fig. 2.** Idem to Figure 1 for  $\alpha_{\text{CE}} = 1.0$ . More points are obtained as a result of increasing the grid resolution in the parameter space. Note that we omitted the lowest efficiencies  $\epsilon \leq 0.2$  since no BBH solutions compatible with GW151226 nor GW170608 were found.



**Fig. 3.** Chirp masses ( $M_{\text{chirp}}$ ) and mass ratios ( $q_{\text{BBH}}$ ) of BBHs compatible with GW151226 and/or GW170608 events (within their 100%, 90% and 68% credible intervals in salmon and blue shaded areas, respectively), that merge within the Hubble time for  $\alpha_{\text{CE}} = 2.0$ . Each panel corresponds to a different value of the MT efficiency. Square (round) markers correspond to binaries with  $M_{\text{BH},2} > M_{\text{BH},1}$  ( $M_{\text{BH},2} < M_{\text{BH},1}$ ). Different point colours correspond to each metallicity adopted in this work (see legend).

### 3.2. Black hole masses

In Figure 3 we present the distribution of BH mass associated with the progenitors found using  $\alpha_{\text{CE}} = 2.0$ . Independently of the MT efficiency, the binaries have  $q_{\text{BBH}} > 0.4$  and cover the entire range in  $M_{\text{chirp}}$ . Larger MT efficiencies tend to form BBHs with mass ratios closer to unity, while  $q_{\text{BBH}} \lesssim 0.7$  for  $\epsilon \leq 0.2$ .

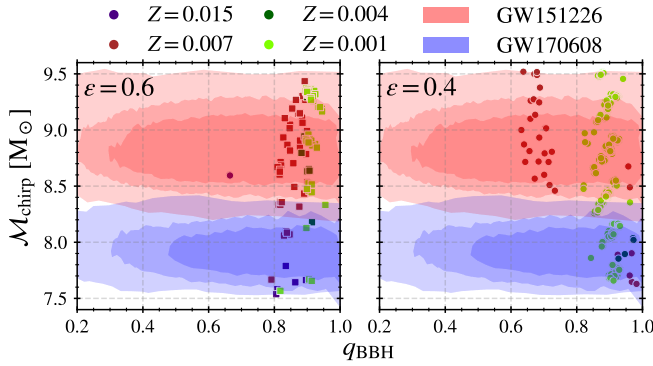


**Fig. 4.** Idem to Figure 3 for  $\alpha_{\text{CE}} = 1.0$ . No BBH solutions compatible with GW151226 nor with GW170608 are found at low efficiencies  $\epsilon \leq 0.2$ , and are omitted here.

BBHs obtained at lower metallicities span the entire range of mass ratios, while  $0.5 \lesssim q_{\text{BBH}} \lesssim 0.8$  for the higher metallicities as a consequence of the high mass loss rates associated with winds. Interestingly, in the latter range of metallicities, for some cases (showed in square markers in Figure 3), the most massive BH is formed last due to the rejuvenation of the secondary (and initially least massive) star during the stable MT stage. Additionally, at low metallicities, such binaries concentrate along lines of decreasing  $M_{\text{chirp}}$  when  $q_{\text{BBH}}$  increases.

In Figure 4 we present BH mass properties obtained with  $\alpha_{\text{CE}} = 1.0$ . All BBH have  $q_{\text{BBH}} > 0.6$ . When  $\epsilon = 0.6$ , the BBH can form at all metallicities. Almost all of them went through a rejuvenation process which produced a secondary BH more massive than the primary. On the other hand, for  $\epsilon = 0.4$  this is only achieved for the lowest metallicities.

### 3.3. Merger time delay

In Figures 5 and 6 we present the distribution of merger time delay  $t_{\text{merger}}$  as a function of  $M_{\text{chirp}}$  for all BBHs with masses compatible to GW151226 and/or GW170608, for  $\alpha_{\text{CE}} = 2.0$  and  $\alpha_{\text{CE}} = 1.0$  respectively. When  $\alpha_{\text{CE}} = 2.0$  BBHs merge after very long delays  $t_{\text{merger}} \gtrsim 100$  Myr, comparable to Hubble time, while, when  $\alpha_{\text{CE}} = 1.0$  the merger occurs with much shorter delays,  $t_{\text{merger}} \lesssim 3$  Gyr, and typically 100 Myr.

Delay times play a fundamental role in determining the age of the stellar population from which the observed BBHs originate. The above results imply that old binary systems are involved in the first set of simulations, while the second favours younger binary systems. However, in this case, high metallicities are strongly disfavoured, putting strong constraints on the expected properties of their possible host galaxies. Thus, merger time delays are strongly impacted by the assumed CE efficiency.

Interestingly, for all simulated binaries, the CE phase is required for the binary to merge within a Hubble time. As expected, the CE phase plays a fundamental role in BBH mergers in the isolated binary channel. More details can be found in Appendix D.

## 4. Population-weighted results

The results obtained so far rely over regularly grids that uniformly sample the space of initial masses and separations. In this section, we produce *population-weighted* results rescaled by empirical initial mass functions (IMF) for the primary and sec-

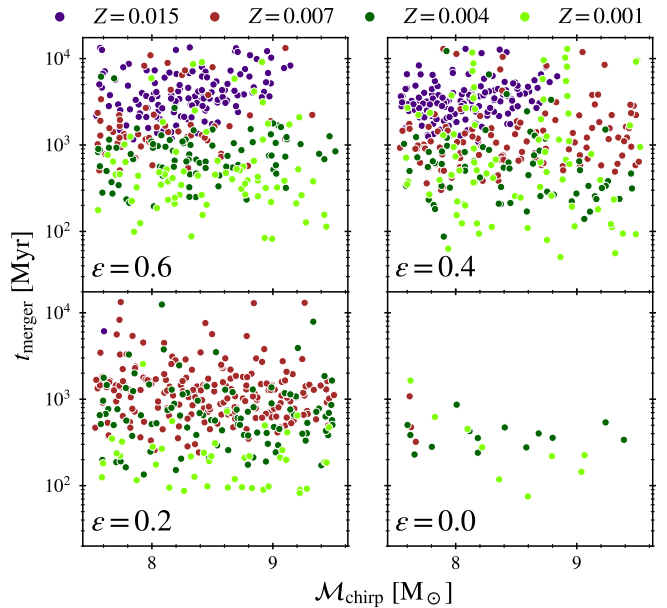


**Fig. 5.** Merger time delay ( $t_{\text{merger}}$ ) of BBHs compatible with GW151226 and/or GW170608 (within their 100% C.I.) for  $\alpha_{\text{CE}} = 2.0$ . Each panel corresponds to different values of the MT efficiency. Different point colours correspond to each metallicity adopted in this work (see legend).

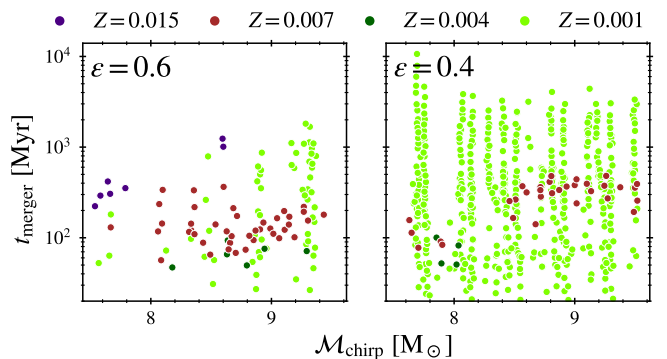


**Fig. 6.** Same as Figure 5 for  $\alpha_{\text{CE}} = 1.0$ . No BBH solutions compatible with GW151226 nor GW170608 are found for the lowest efficiencies  $\epsilon \leq 0.2$  which are thus omitted here.

ondary stars and by an initial separation distribution computed from the observed binary orbital period  $\mathcal{P}$  distributions.

### 4.1. Assumptions and methodology

For the mass  $M_{i,1}$  of the primary and initially most massive star, we use the IMF from Kroupa et al. (1993)

$$\xi(M) \propto \begin{cases} (M/M_0)^{-\alpha_0} & M_{\text{low}} \leq M < M_0 \\ (M/M_0)^{-\alpha_1} & M_0 \leq M < M_1 \\ (M_1/M_0)^{-\alpha_1} (M/M_1)^{-\alpha_2} & M_1 \leq M \leq M_{\text{high}} \end{cases} \quad (3)$$

where  $\alpha_0 = 1.3$ ,  $\alpha_1 = 2.2$  and  $\alpha_3 = 2.7$ , while  $M_{\text{low}} = 0.08 \text{ M}_{\odot}$ ,  $M_0 = 0.5 \text{ M}_{\odot}$ ,  $M_1 = 1 \text{ M}_{\odot}$  and  $M_{\text{high}} = 150 \text{ M}_{\odot}$ .

Given  $M_{i,1}$ , the mass  $M_{i,2}$  of the secondary star is drawn from a flat distribution in the mass ratio  $q = M_{i,2}/M_{i,1}$ ,

$$\xi(q) = \frac{1}{q_{\max} - q_{\min}}, \quad (4)$$

where  $q_{\min} = 0.1$  and  $q_{\max} = 1.0$ .

The initial separation is drawn from the orbital period distribution given in Sana et al. (2012),

$$\xi(\mathcal{P}) \propto \mathcal{P}^{-0.55}, \quad \text{for } 0.15 < \mathcal{P} < 5.5 \quad (5)$$

where  $\mathcal{P} = \log P_{\text{orb}}$  in units of days.

Although orbital properties seem to be relatively unaffected by metallicity in the range between the Milky Way and the Large Magellanic Cloud metallicities (Almeida et al. 2017), throughout this work we assume that these distributions are preserved for the entire range of metallicities.

For each metallicity  $Z$  and MT efficiency  $\epsilon$ , we randomly draw  $10^7$  binaries from the distributions described above. To get a reasonable resolution, we restrict the random draws to the relevant ranges of masses and separations and keep track of the normalisation constant to account for the rest of the distributions, that is otherwise ignored in the Monte-Carlo simulation.

A massive star binary corresponds to a point in the parameter space defined by  $M_{i,1}$ ,  $M_{i,2}$  and  $a_i$ . This point is mapped to the closest point in the regular grid introduced in Sec. 2.5. We assign to the randomly generated binary the properties of the closest binary evolved through the MESA simulations presented in Sec. 2.

This method allows us to obtain statistics representative of the entire binary star population, similarly to population synthesis studies. Contrarily to the latter, our results are however based on a detailed and fully numerical simulation of the binary stellar evolution. Such detailed treatment is usually not considered in standard population synthesis simulations as it is computationally expensive.

## 4.2. Population-weighted results for GW151226 and GW170608

### 4.2.1. Properties of the initial binary

Figures 7 and 8 present the probability distributions for the parameters of the initial stellar binaries that eventually evolve in BBHs compatible with GW151226 and GW170608 assuming  $\alpha_{\text{CE}} = 2.0$  and  $\alpha_{\text{CE}} = 1.0$ , respectively. On the left and in the middle, the panels display the component masses  $M_{i,1}$  and  $M_{i,2}$  of the initial binary, while the panels on the right show the initial separations  $a_i$ . From top to bottom, we show the results obtained with different MT efficiencies.

Progenitors at solar-like metallicity ( $Z = 0.015$ , violet) are only found at high MT efficiencies  $\epsilon > 0.4$ . In the fully inefficient case  $\epsilon = 0$ , the only possible progenitors are at low-metallicity  $Z < 0.004$ . Because of the mass loss due to stellar winds, higher initial masses are needed when the metallicity increases to produce BHs with the proper target mass.

### 4.2.2. Properties of the binary black holes

Figures 9 and 10 show the parameter distributions of the formed BBH when they are compatible with GW151226 and GW170608 assuming  $\alpha_{\text{CE}} = 2.0$  and  $\alpha_{\text{CE}} = 1.0$ , respectively.

When  $\alpha_{\text{CE}} = 2.0$  and  $\epsilon \geq 0.4$ , the smaller the metallicity the larger the mass of the secondary BH. When  $Z$  decreases, the distribution peak in the mass ratio  $q_{\text{BBH}} = M_{\text{BH},2}/M_{\text{BH},1}$  shifts toward unity, and even exceeds 1 for the lowest metallicity  $Z = 0.001$  and  $\epsilon = 0.6$ . For lower MT efficiencies  $\epsilon \leq 0.2$ ,  $q_{\text{BBH}} \sim 0.5 - 0.75$  with no clear dependence on the metallicity.

The chirp mass  $\mathcal{M}_{\text{chirp}}$  distribution basically spans the entire 100% C.I. for both GW events, independently of the MT efficiency and metallicity. For the largest MT efficiency  $\epsilon = 0.6$ , we

note a slight preference  $\mathcal{M}_{\text{chirp}} \sim 8.3 \text{ M}_\odot$ . The narrow distribution obtained for  $\epsilon = 0$  and  $Z = 0.007$  is not reliable, due to the very low statistics available in this case.

When  $\alpha_{\text{CE}} = 1.0$ , the binary evolution leads to almost equal-mass binaries. The secondary BH is clearly the heaviest ( $q_{\text{BBH}} > 1$ ) when the MT efficiency is large,  $\epsilon = 0.6$ . The chirp mass  $\mathcal{M}_{\text{chirp}}$  tends to decrease for larger metallicities when  $\epsilon = 0.6$ , while  $Z$  has little impact on  $\mathcal{M}_{\text{chirp}}$  when  $\epsilon = 0.4$ .

### 4.2.3. Merger time delay

Fig. 11 presents the distribution of the merger time delay  $t_{\text{merger}}$ . When  $\alpha_{\text{CE}} = 2.0$  and  $\epsilon > 0$ ,  $t_{\text{merger}}$  clearly increases with metallicity. The distribution peak goes from  $\sim 300$  Myr to 10 Gyr when  $Z$  spans the selected metallicity range, from 0.001 to 0.015. This correlation disappears for fully inefficient MT,  $\epsilon = 0$  and, in this case,  $t_{\text{merger}} \lesssim 1$  Gyr are obtained. When  $\alpha_{\text{CE}} = 1.0$ , we observe the same relationship between  $t_{\text{merger}}$  and  $Z$ . The merger time delay is however reduced by a factor  $\sim 10$  with respect to the previous CE efficiency. The merger time delays are thus strongly impacted by the metallicity and the CE phase efficiency.

## 5. Merger rate and gravitational-wave events

We use the population-weighted samples presented in the previous section to estimate the local merger density rate leading to GW events comparable to those studied in this work.

### 5.1. Method

For binary distributions given by  $dN = f_j(M_{i,1}, M_{i,2}, a_i) dx_j$  our weighted simulations provide the number density of binaries in the multidimensional space defined by the initial masses, separations and delay times ( $t_m = T + t_{\text{merger}} \approx t_{\text{merger}}$ , where  $T \lesssim 10$  Myr is the binary lifetime) which produce each specific GW event, defined as:

$$\frac{dN}{dM_{i,1} dM_{i,2} da_i dt_m}(M_{i,1}, M_{i,2}, a_i; t_m) = P_{\text{GW-event}} f_{M_{i,1}} f_{M_{i,2}} f_{a_i} \delta[t(z) - (t_m + t')] dt_m da_i dM_{i,2} dM_{i,1} dt' \quad (6)$$

where  $P_{\text{GW-event}}$  is a Kronecker-delta function that selects binaries which evolve into BBHs compatible with the considered GW events.

By assuming a cosmology that relates the redshift  $z$  to the cosmic time  $t$ , the intrinsic GW event rate  $\mathcal{R}(Z, z(t))$  can be obtained by integration over the full parameter space:

$$\mathcal{R}(Z, z(t)) = \mathcal{N}_{\text{corr}} \int_0^{t(z)} \int_{M_{i,1}} \int_{M_{i,2}} \int_{a_i} \int_0^{t(z)} \frac{dN}{dM_{i,1} dM_{i,2} da_i dt_m} \widehat{\text{SFR}}(t'; Z) \delta[t(z) - (t_m + t')] dt_m da_i dM_{i,2} dM_{i,1} dt' \quad (7)$$

where  $\mathcal{N}_{\text{corr}}$  is a normalisation factor that includes the total mass  $\mathcal{M}_{\text{T}}$  of the  $10^7$  simulated binaries, and takes into account the initial masses ( $\mathcal{N}_{\text{IMF}}$ ), mass ratios ( $\mathcal{N}_q$ ) and separations ( $\mathcal{N}_a$ ) excluded from the Monte-Carlo simulation

$$\mathcal{N}_{\text{corr}} = \frac{\mathcal{N}_a \mathcal{N}_{\text{IMF}}}{\mathcal{N}_q(f_b)} \frac{1}{\mathcal{M}_{\text{T}}}; \quad (8)$$

where we assume that binary systems represent half the total number of stars i.e.,  $f_b = 0.5$ .

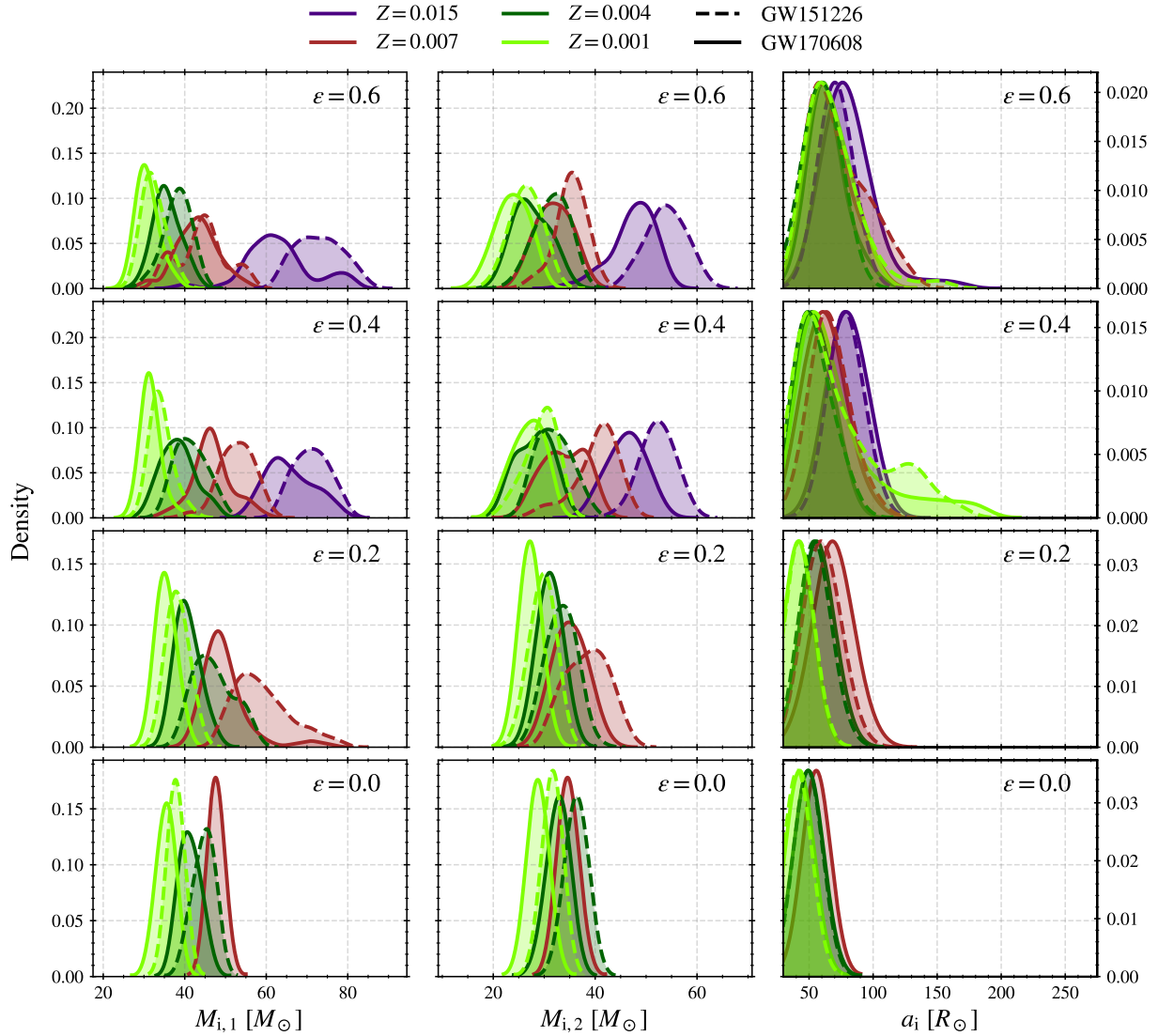


**Fig. 7.** Population-weighted probability distributions for the parameters of the initial star binaries that eventually evolve in BBHs compatible with GW151226 (dashed) and GW170608 (solid) assuming  $\alpha_{\text{CE}} = 2.0$ . Left and middle panels show the component masses  $M_{i,1}$  and  $M_{i,2}$  of the initial binary and its initial separation  $a_i$  on the right. From top to bottom, the panels correspond to different MT efficiencies. Colours correspond to the metallicities given in the legend.

$\widehat{\text{SFR}}(t'; Z)$  is the metallicity-dependent star formation rate, namely

$$\widehat{\text{SFR}}(t'; Z) = \text{SFR}(t')\psi(Z, z'(t')) \quad (9)$$

where  $\text{SFR}(t')$  is the total star formation rate history at binary-formation time  $t'$  in co-moving coordinates (which we adopt from Strolger et al. 2004), and  $\psi(Z, z'(t'))$  accounts for the fraction of stars formed at metallicity  $Z$ .

We divide the full metallicity range into four intervals, namely  $\Delta Z = 0\text{--}0.0025$ ,  $0.0025\text{--}0.005$ ,  $0.005\text{--}0.0075$ , and  $0.0075\text{--}0.03$ , which we assign to the four simulated values ( $Z = 0.001, 0.004, 0.007$ , and  $0.015$ , see Sec. 2). We then compute  $\Psi(\Delta Z, z') = \int_{\Delta Z} \psi(Z, z') dZ$ , where  $\psi$  is normalised to unity, such that  $\int_0^\infty \psi(Z, z') dZ = 1$  at redshift  $z'$  (Langer & Norman 2006).

Thanks to the  $\delta$  function in Eq. (7), the summation runs over binary systems at redshift  $z(t)$  with appropriate formation time  $t'$  and merging delay times  $t_m$  and that evolve into BBH merging at cosmic time  $t(z)$ . In practice, this integral is evaluated by counting the fraction of sampled binaries per total simulated mass,

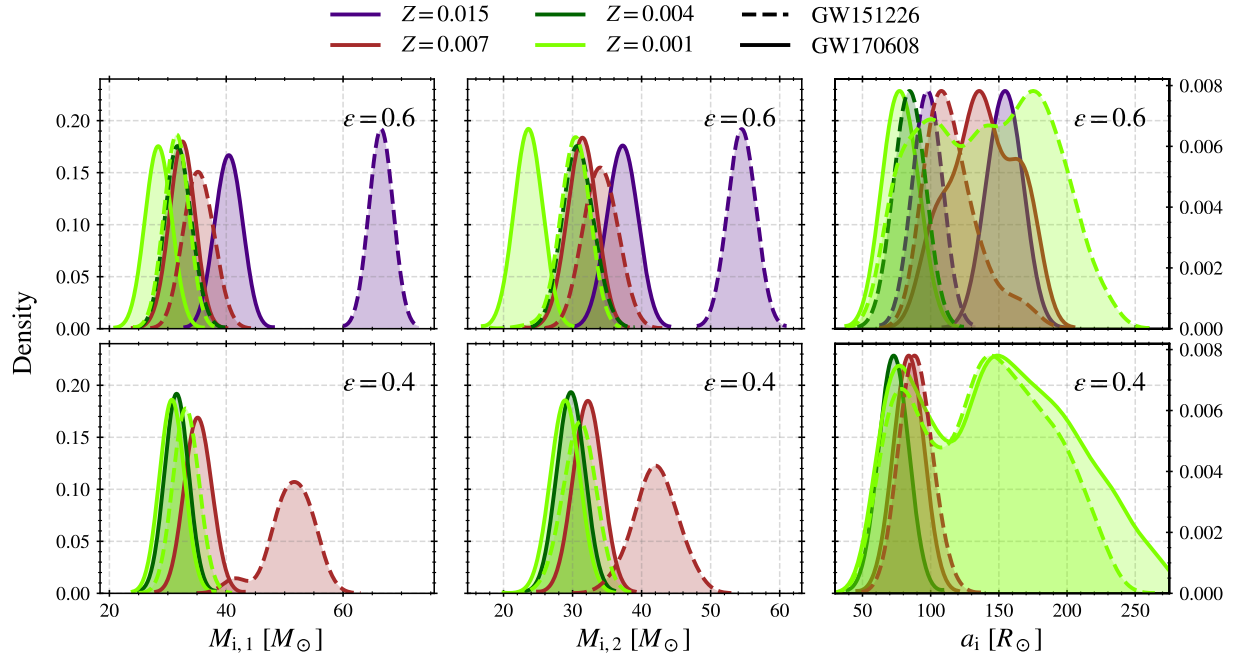
$M_T$ , that lead to a BBH merger at the expected redshift or cosmic time. The formation time and delay times are binned with a resolution of 100 Myr.

## 5.2. Application

Figure 12 shows the dependency of the merger rate density  $\mathcal{R}$  with the metallicity of the progenitor population and Table 2 compares the local merger rate densities  $\mathcal{R}(z = 0)$ , that are relevant for predicting GW event rates.

The expected local merger rate densities are all larger for  $\alpha_{\text{CE}} = 2.0$ . This is consistent to the smaller parameter space allowed for the binary progenitors as shown in Figs 1 and 2. The only exception is  $\epsilon = 0.4$  and  $Z = 0.001$ , where the local rate densities is 40 % larger when  $\alpha_{\text{CE}} = 1.0$  and reaches  $\mathcal{R}(z = 0) = 0.4 \text{ yr}^{-1} \text{ Gpc}^{-3}$ . As a direct consequence of the chemical evolution, the merger rate decays rapidly at high redshift for the larger metallicities, independently of  $\alpha_{\text{CE}}$ .

When  $\alpha_{\text{CE}} = 2.0$ ,  $\mathcal{R}(z = 0) \gtrsim 0.1 \text{ yr}^{-1} \text{ Gpc}^{-3}$  for  $\epsilon \geq 0.4$  with comparable contributions from all metallicities. However

**Fig. 8.** Idem to Figure 7 for  $\alpha_{\text{CE}} = 1.0$ .**Table 2.** Merger rate density at zero redshift for each GW event and  $\alpha_{\text{CE}}$ . Units are in  $\text{yr}^{-1} \text{Gpc}^{-3}$ 

GW151226			GW170608		
$\epsilon$	$Z$	$\alpha_{\text{CE}} = 2$	$\alpha_{\text{CE}} = 1$	$\alpha_{\text{CE}} = 2$	$\alpha_{\text{CE}} = 1$
0.6	0.015	0.202	0.004	0.347	0.050
	0.007	0.082	0.123	0.214	0.054
	0.004	0.143	0.025	0.186	0.005
	0.001	0.208	0.088	0.125	0.015
0.4	0.015	0.136	—	0.366	—
	0.007	0.138	0.028	0.136	0.019
	0.004	0.136	—	0.213	0.018
	0.001	0.343	0.440	0.263	0.401
0.2	0.015	—	—	0.009	—
	0.007	0.121	—	0.148	—
	0.004	0.102	—	0.116	—
	0.001	0.043	—	0.030	—
0.0	0.015	—	—	—	—
	0.007	—	—	0.004	—
	0.004	0.007	—	0.017	—
	0.001	0.007	—	0.009	—

the local rate densities steeply decrease below this level at lower MT efficiencies, with a reduction by two orders of magnitude in the extreme case,  $\epsilon = 0$ . In the case of  $\alpha_{\text{CE}} = 1.0$ ,  $\mathcal{R}(z = 0)$  is largely dominated by the lowest metallicities independently of the MT efficiency.

### 5.3. Implications for O1 and O2 science runs

We apply the relation from Dominik et al. (2015) to rescale the intrinsic merger rate from (7) into GW detection rates:

$$R_D = \frac{4\pi}{3} D_h^3 \langle w^3 \rangle \langle (\mathcal{M}_c / 1.2 M_\odot)^{15/6} \rangle \mathcal{R}(z = 0) \quad (10)$$

**Table 3.** Detection rates for O1 and O2 observing runs calculated using relation from Dominik et al. (2015) for each GW event and  $\alpha_{\text{CE}}$ , and considering  $D_h = 100 \text{ Mpc}$ .

GW151226		GW170608		
$\epsilon$	$\alpha_{\text{CE}} = 2$	$\alpha_{\text{CE}} = 1$	$\alpha_{\text{CE}} = 2$	
0.6	0.398 $\text{yr}^{-1}$	0.151 $\text{yr}^{-1}$	0.406 $\text{yr}^{-1}$	0.058 $\text{yr}^{-1}$
0.4	0.473 $\text{yr}^{-1}$	0.292 $\text{yr}^{-1}$	0.455 $\text{yr}^{-1}$	0.204 $\text{yr}^{-1}$
0.2	0.167 $\text{yr}^{-1}$	—	0.141 $\text{yr}^{-1}$	—
0.0	0.009 $\text{yr}^{-1}$	—	0.014 $\text{yr}^{-1}$	—

where  $w$  is a geometrical factor,  $\mathcal{M}_c$  is the chirp mass of the BBH,  $D_h$  is the horizon distance and  $\mathcal{R}$  is the merger rate density evaluated at  $z = 0$ .

Consistently to the highest range for BNS obtained by advanced LIGO and advanced Virgo during their previous science run O2, we consider a binary neutron star (BNS) range  $D_h = 100 \text{ Mpc}$  averaged over all sky directions. We also study how these rates improve with the current observing run O3, during which  $D_h = 140 \text{ Mpc}$ <sup>3</sup>.

The results are shown in Fig. 13 and Table 3. The highest rates are obtained for the highest MT efficiencies ( $\epsilon = 0.4$  and  $0.6$ ) for both CE cases. For the lowest MT efficiencies, the outcome rates are significantly smaller. In the high CE efficiency case, the rates decrease by a factor of 4–5, while for the low CE efficiency no progenitors are found. Thus, in general, the highest MT efficiency cases are favoured.

In Appendix E, we explore the dependence of the event rates on the assumed star formation history. We find that the strongest differences in event rates are introduced by the metallicity distribution. On the contrary, different SFR histories produce similar outcome rates. These results are compatible with those from Chruslinska & Nelemans (2019) and Neijssel et al. (2019).

<sup>3</sup> See [https://www.gw-openscience.org/detector\\_status/](https://www.gw-openscience.org/detector_status/) for more information.

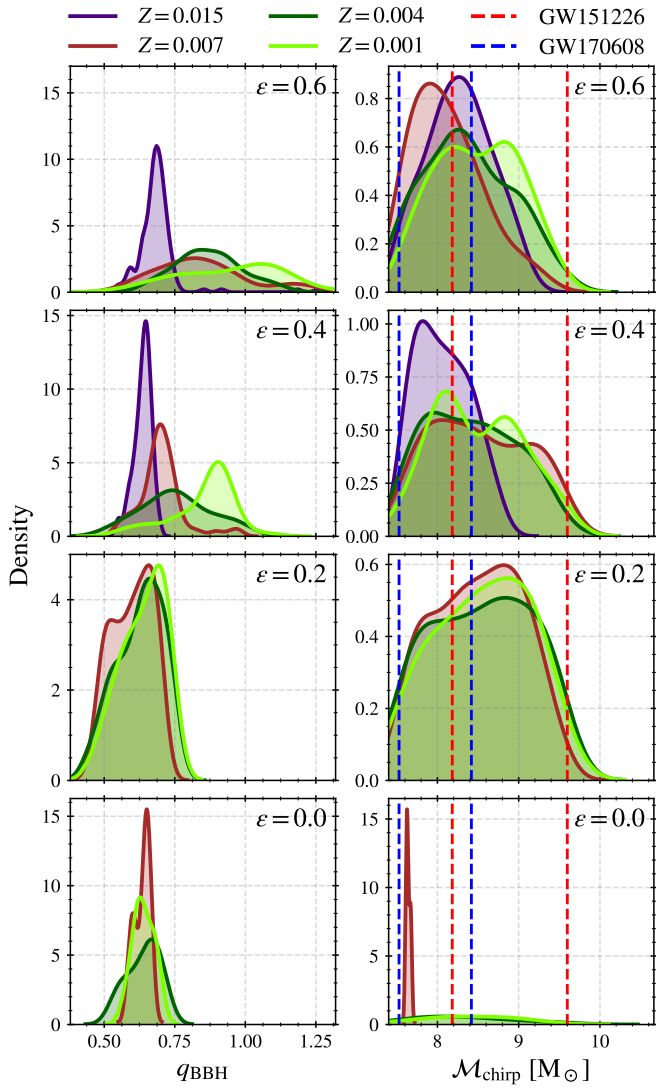


**Fig. 9.** Population-weighted probability distributions for the parameter of the BBHs compatible with GW151226 and/or GW170608 assuming  $\alpha_{\text{CE}} = 2.0$ . Left and right panels correspond to mass ratio and chirp mass, respectively. From top to bottom, the panels correspond to different MT efficiencies. Colours correspond to the metallicities given in the legend. The vertical dashed lines indicate the 100% C.I. of  $M_{\text{chirp}}$  of GW151226 (red) and GW170608 (blue).

## 6. Discussion

In this work we have studied the progenitor properties for the two least-massive BBH mergers (GW151226 and GW170608) detected during the first two science runs of Advanced LIGO and Advanced Virgo, assuming they formed through the so-called isolated binary evolution channel. We simulated a large set of non-rotating stellar models using the binary stellar evolution code MESA (see Appendix B). We investigated a wide range of initial stellar masses, separations and metallicities. Moreover, to analyse the impact of unconstrained phases of binary evolution related to stellar interactions, we examined the dependence of the outcome results on different efficiencies for stable MT and CE ejection.

In the high CE efficiency scenario ( $\alpha_{\text{CE}} = 2.0$ ), we found progenitors leading to BBH compatible with both GW events, for all considered MT efficiencies. Their initial masses lie in the  $25-90 \text{ M}_\odot$  mass range for the primary (more massive) star and

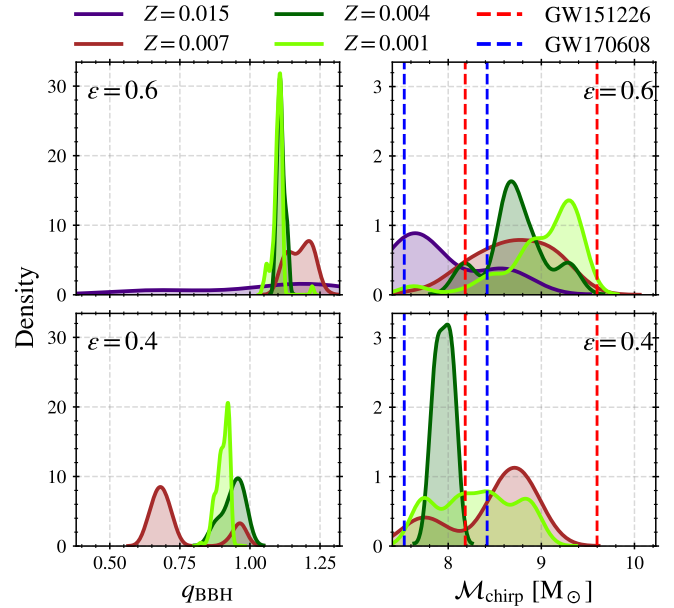


**Fig. 10.** Same as Figure 9 for  $\alpha_{\text{CE}} = 1.0$ .

in the  $20-60 \text{ M}_\odot$  range for the secondary star. The initial separations are bound to the region  $40-200 \text{ R}_\odot$ . The initial mass ranges depend strongly on the stellar metallicity. This is a direct consequence of the stellar wind efficiencies as pointed out by other authors (e.g., Giacobbo & Mapelli 2018; Kruckow et al. 2018).

The results obtained in high CE efficiency regime are consistent with other studies of the literature based on different approaches. At low metallicity  $Z = 0.001$ , our results are consistent with Fig. 1 from Stevenson et al. (2017). Furthermore, we obtain similar ranges for the progenitor masses for  $Z = 0.004$  as Kruckow et al. (2018). Although our highest metallicity differs, our progenitors for GW151226 fall in the same mass range, i.e.,  $M_{i,1} \sim 80 \text{ M}_\odot$  and  $55 \lesssim M_{i,2} \lesssim 60 \text{ M}_\odot$  when the highest MT efficiency is assumed (it is worth mentioning that different MT and CE efficiencies were used). Moreover, we find that the BH masses for GW151226 are at the maximum limit achievable at the highest metallicity  $Z = 0.015$ .

In the low CE efficiency regime ( $\alpha_{\text{CE}} = 1.0$ ) we obtain a narrower range of initial masses, favouring cases where initial masses are close to equal ( $q \sim 1$ ), while initial separations tend to be shifted to higher values, see Fig. 2. In this case a clear relation between the progenitor masses and the metallicity of the population is also recovered. We obtain several solutions for our lowest metallicity, which can be related to a stability region even though the finer step used in the exploration grid should also be considered.

We find that all these binary systems undergo a CE phase when the primary star has already collapsed to a BH, as expected in the standard BBH formation scenario (Belczynski et al. 2002; Voss & Tauris 2003; Tauris & van den Heuvel 2006; Dominik et al. 2012; Belczynski et al. 2016). Although CE phases triggered while the donor star is in the Hertzsprung gap when the star does not have a well-defined core-envelope structure (Ivanova & Taam 2004) are usually assumed to lead to a CE merger (Dominik et al. 2012; Spera et al. 2019), by means of our detailed MT treatment (still 1D numerical simulations) we find regions of the explored parameter space populated with binary systems that survive such phase. Our simulations show that these low-mass BBHs can only merge in timescales smaller than the Hubble time

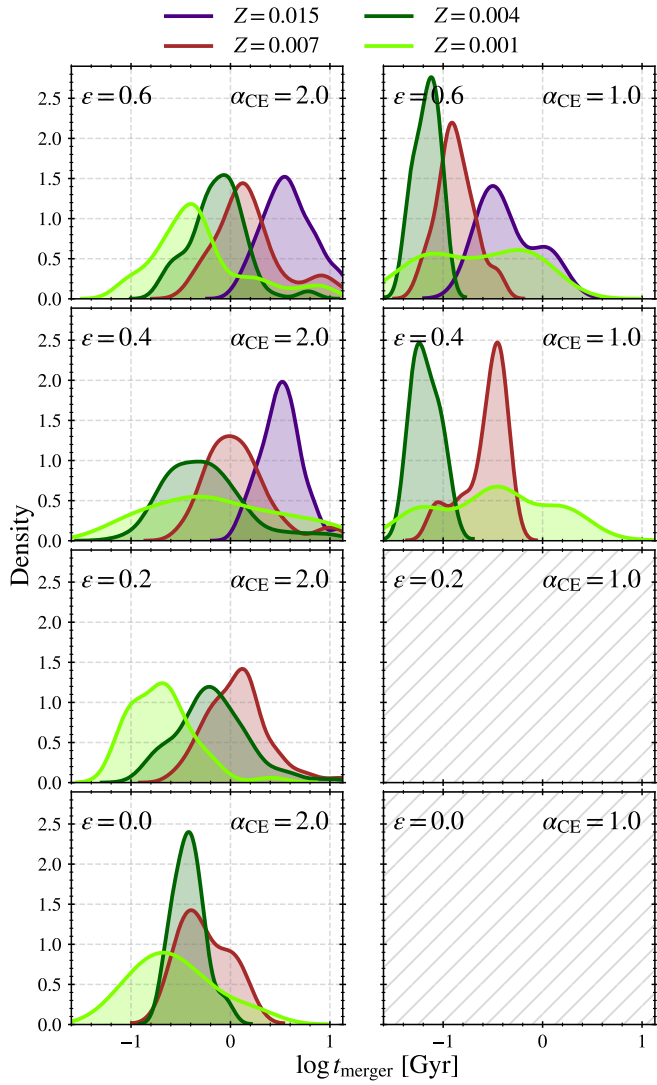


**Fig. 11.** Population-weighted probability distribution of merger time delay ( $t_{\text{merger}}$ ) of BBHs compatible with GW151226 and/or GW170608 (within their 100% C.I.). Left (right) panels correspond to  $\alpha_{\text{CE}} = 2.0$  ( $\alpha_{\text{CE}} = 1.0$ ). Top to bottom panels present different values of the MT efficiency adopted throughout this work. Different colours correspond to each metallicity value (see legend). Hatched panels represent values of efficiencies where no BBHs compatibles with GW151226 nor GW170608 were found.

if they experience a CE phase enabling the ultra-compact binary formation (see also Appendix D).

Additionally, assuming appropriate distributions for the initial-mass function, binary mass ratios and separations, we calculated the merger rates associated to each GW event for the explored metallicities, which could arise from different formation environments. In the case of  $\alpha_{\text{CE}} = 2.0$ , for the two highest MT efficiencies we are not able to rule out any metallicity as a possible progenitor, while in the lower part of MT efficiencies we expect low-metallicity progenitors to dominate. On the other hand, simulations with  $\alpha_{\text{CE}} = 1.0$  are more likely to be dominated by low-metallicity values. We find that a decrease in the CE ejection efficiency tends to produce lower rates; with the exception of just two cases:  $\epsilon = 0.6$  and  $Z = 0.007$  or  $\epsilon = 0.4$  and  $Z = 0.001$ .

Care must be taken when comparing our derived rates with other works because our focus is set on the detection rate of two

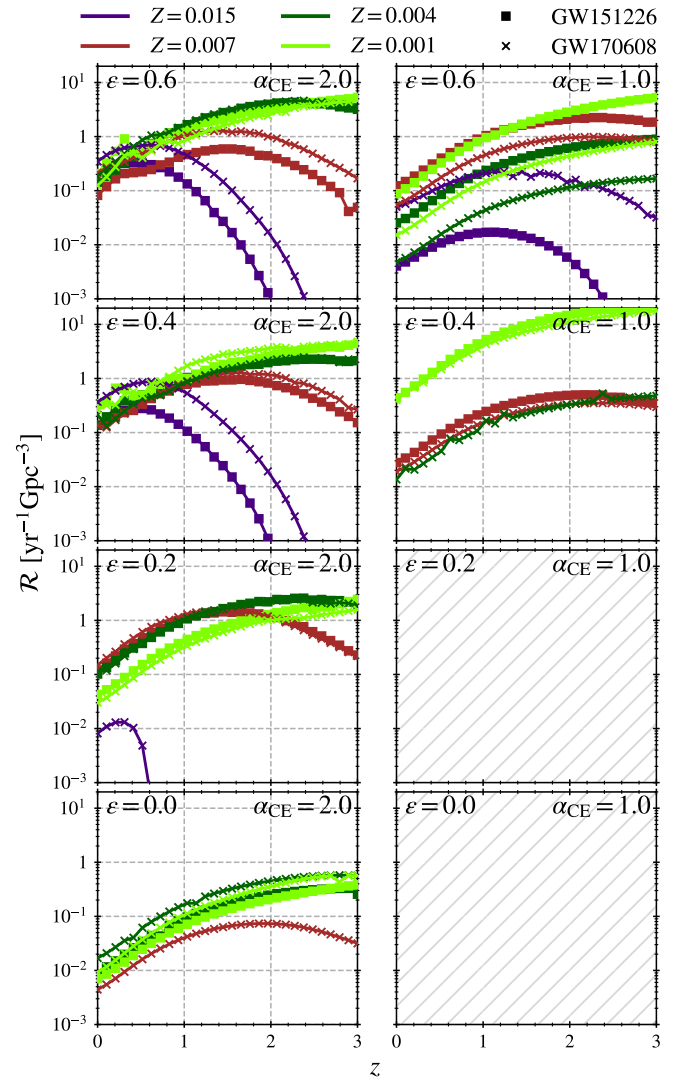


**Fig. 12.** Merger rate density history of events compatible with GW151226 (cross markers) and GW170608 (square markers) as a function of redshift for each metallicity value adopted in this work (see legend for colours). Left panel (right panel) corresponds to simulations performed using  $\alpha_{\text{CE}} = 2.0$  ( $\alpha_{\text{CE}} = 1.0$ ). From top to bottom panels we show results for different MT efficiencies studied in this work. Hatched panels are the cases where no BBHs compatible with GW151226 nor GW170608 are found.

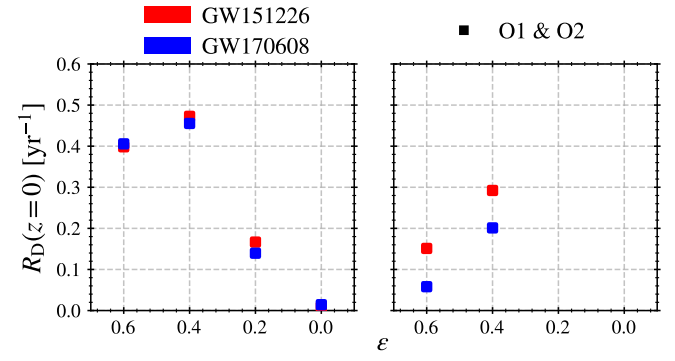


**Fig. 13.** Total detection rates,  $R_D(z = 0)$ , marginalised over metallicity, as a function of MT efficiency  $\epsilon$  for  $\alpha_{\text{CE}} = 2.0$  (left panel) and  $\alpha_{\text{CE}} = 1.0$  (right panel) of events compatible with GW151226 (red) and GW170608 (blue) within their 100% credible intervals. Filled squares are detection rates of O1 and O2 LVC observing runs.

particular GW events. For the full BBH population, the LVC reported an empirical rate of  $\mathcal{R} \simeq 12 - 213 \text{ yr}^{-1} \text{ Gpc}^{-3}$  (Abbott et al. 2017c), which is naturally higher than the values reported in this work. Our derived detection rates at instrumental sensitivity of Advanced LIGO-Virgo detectors are below one event per year, which is consistent with the actual GW events. In our simulations with  $\alpha_{\text{CE}} = 2.0$  and for the highest MT efficiencies, we obtain rates which are consistent with those found by Kruckow et al. (2018). However, in such cases we also find a comparable rate at lower metallicities, which prevent us from distinguishing the progenitor according to the metal content of the formation environment. In our simulations, the highest MT efficiency cases are favoured, independently of the CE efficiency and the stellar formation history.

Finally, we caution that all of these rates are subject to several uncertainties: when using different values in the input physical parameters, rates can vary by an order of magnitude. For example, it might be unlikely that the efficiency during MT phases remains the same throughout the entire evolution, as rotation might limit accretion from the companion (Packet 1981; Paczynski 1991; Popham & Narayan 1991). Moreover, the uncertainties in the evolution of metallicity and the star formation rate history were shown to have a strong impact on the BBH merger rates (see, for instance, Neijssel et al. 2019, and our Appendix E).

## 7. Summary and conclusions

Before summarising the results of our paper, we would like to point out the particular approach of our work: instead of going through more numerous but less detailed modelling as in binary population synthesis (see references in Section 1), we performed more than 50 000 simulations of binary evolution with the 1D-hydrodynamic MESA code, to study the formation history, progenitor properties and expected rates of the two lowest-mass BBH mergers detected during the O1 and O2 campaigns of LIGO-Virgo.

To compute the whole evolution of the binary, we modified the MESA code, to include *i.* the BH formation (through instantaneous, spherically symmetric ejection of the H/He stellar envelope and *ii.* the computation of unstable mass transfer during the CE phase (with two values of the efficiency parameter  $\alpha_{\text{CE}}$ : 1.0 and 2.0).

We summarise below the main results achieved in this work:

- General remarks:** stellar progenitors of GW 151226 are more massive than those of GW 170608 (in agreement with the final masses of the black holes); higher initial orbital separation  $a_i$  implies longer merger times  $t_{\text{merger}}$ ; higher metallicity  $Z$  implies more massive progenitors (due to mass lost through stellar winds); for inefficient mass transfer efficiency ( $\epsilon < 0.2$ ), only low  $Z$  ( $< 0.004$ ) binaries can become progenitors, and for high MT efficiency ( $\epsilon \geq 0.4$ ), we obtain either solar metallicity progenitors of different masses, or low  $Z$  progenitors evolving towards similar mass stars (mass ratio  $q$  close to unity, due to rejuvenation process, where the second-formed BH becomes more massive than –or at least as massive as– the first); In the case of low CE efficiency ( $\alpha_{\text{CE}} = 1.0$ ), we obtain progenitors having  $q$  close to unity (rejuvenation), binaries with  $a_i \leq 60M_\odot$  merge during the CE phase, and we do not find any BBH solution for  $\epsilon \leq 0.2$ .
- Mass ratio and chirp masses:**  $q_{\text{BBH}}$  is always  $> 0.4$ , covering all the  $M_{\text{chirp}}$  range; high MT ( $\epsilon \geq 0.4$ ) tend to form BBH with  $q_{\text{BBH}}$  closer to 1, while  $q_{\text{BBH}} \leq 0.75$  for low MT ( $\epsilon \leq 0.2$ ). Low metallicity stars span whole range of  $q_{\text{BBH}} =$

[0.5 – 1.25], with larger mass of secondary BH in some cases, and decreasing  $M_{\text{chirp}}$  when  $q_{\text{BBH}}$  increases, while high metallicity stars span a shorter range  $q_{\text{BBH}} = [0.5 – 0.8]$  (only high  $Z$  stars which are rejuvenated lead to  $q_{\text{BBH}} \sim 1$ ). For  $\alpha_{\text{CE}} = 1.0$ , progenitors tend towards equal-mass binaries, all BBH having  $q_{\text{BBH}} > 0.6$  at all  $Z$ , and even  $q_{\text{BBH}} > 0.8$  for  $\epsilon = 0.6$  (rejuvenation process).

- Merger time delay:** for  $\alpha_{\text{CE}} = 2.0$ ,  $t_{\text{merger}}$  increases with metallicity  $Z$ , from 300 Myr to 10 Gyr (no correlation though for  $\epsilon = 0$ , for which  $t_{\text{merger}} \leq 1$  Gyr), while for  $\alpha_{\text{CE}} = 1.0$   $t_{\text{merger}}$  is much shorter (due to late ejection of CE), from 10 Myr to  $\leq 3$  Gyr (typical value of 100 Myr); There exists a dichotomy between an old merger population made of high  $Z$  progenitors, and a young merger population constituted of low  $Z$  progenitors; The merger time delay is strongly impacted by both the metallicity and the assumed CE efficiency, the CE phase being always required for binaries to merge within the Hubble time.
- Merger rate density:** Local merger rate densities are all larger for  $\alpha_{\text{CE}} = 2.0$  than  $\alpha_{\text{CE}} = 1.0$  (only for  $\epsilon = 0.4$  and  $Z = 0.001$  is  $\mathcal{R}$  40% higher for  $\alpha_{\text{CE}} = 1.0$  than for  $\alpha_{\text{CE}} = 2.0$ );  $\mathcal{R}$  decays rapidly at high redshift for large metallicity (due to chemical evolution of the universe), independently of  $\alpha_{\text{CE}}$ . For  $\alpha_{\text{CE}} = 2.0$ ,  $\mathcal{R} > 0.1$  for  $\epsilon > 0.2$  and  $Z < 0.015$ ; For  $\alpha_{\text{CE}} = 1.0$ ,  $\mathcal{R}$  is largely dominated by low  $Z$ , independently of MT rate.

On a future work we plan to extend the range of masses of the binary progenitors studied here in order to explore the low-mass end of BH formation, and its transition to neutron stars, which could lead to a mass gap in the compact object masses, which might be probed with GW observations of BBHs.

**Acknowledgements.** This work was supported by the LabEx UnivEarthS, Interface project I10, “From evolution of binaries to merging of compact objects”. We acknowledge use of Arago Cluster from Astroparticule et Cosmologie (APC) for our calculations. ASB is a CONICET fellow. We are grateful to the MESA developers for building and making available high-quality computational software for astrophysics.

**Software:** **MESA:** Modules for Experiments in Stellar Astrophysics<sup>4</sup>, ipython/jupyter (Perez & Granger 2007), matplotlib (Hunter 2007), NumPy (van der Walt et al. 2011), scipy (Jones et al. 2001–) and Python from python.org. This research made use of astropy, a community-developed core Python package for astronomy (Astropy Collaboration et al. 2013, 2018).

## References

- Abbott, B. P., Abbott, R., Abbott, T. D., et al. 2016, Phys. Rev. Lett., 116, 241103  
 Abbott, B. P., Abbott, R., Abbott, T. D., et al. 2019a, Physical Review X, 9, 031040  
 Abbott, B. P., Abbott, R., Abbott, T. D., et al. 2019b, ApJ, 882, L24  
 Abbott, B. P., Abbott, R., Abbott, T. D., et al. 2017a, Phys. Rev. Lett., 119, 161101  
 Abbott, B. P., Abbott, R., Abbott, T. D., et al. 2017b, ApJ, 851, L35  
 Abbott, B. P., Abbott, R., Abbott, T. D., et al. 2017c, Phys. Rev. Lett., 118, 221101  
 Almeida, L. A., Sana, H., Taylor, W., et al. 2017, A&A, 598, A84  
 Astropy Collaboration, Price-Whelan, A. M., Sipőcz, B. M., et al. 2018, AJ, 156, 123  
 Astropy Collaboration, Robitaille, T. P., Tollerud, E. J., et al. 2013, A&A, 558, A33  
 Bae, Y.-B., Kim, C., & Lee, H. M. 2014, MNRAS, 440, 2714  
 Belczynski, K., Holz, D. E., Bulik, T., & O’Shaughnessy, R. 2016, Nature, 534, 512  
 Belczynski, K., Kalogera, V., & Bulik, T. 2002, ApJ, 572, 407  
 Belczynski, K., Kalogera, V., Rasio, F. A., et al. 2008, ApJS, 174, 223  
 Bhattacharya, D. & van den Heuvel, E. P. J. 1991, Phys. Rep., 203, 1  
 Böhm-Vitense, E. 1958, ZAp, 46, 108

<sup>4</sup> <http://mesa.sourceforge.net/>

- Braun, H. & Langer, N. 1995, A&A, 297, 483  
 Brott, I., Evans, C. J., Hunter, I., et al. 2011, A&A, 530, A116  
 Chruslinska, M. & Nelemans, G. 2019, MNRAS, 488, 5300  
 de Jager, C., Nieuwenhuijzen, H., & van der Hucht, K. A. 1988, A&AS, 72, 259  
 de Kool, M. 1990, ApJ, 358, 189  
 Dominik, M., Belczynski, K., Fryer, C., et al. 2012, ApJ, 759, 52  
 Dominik, M., Berti, E., O'Shaughnessy, R., et al. 2015, ApJ, 806, 263  
 Dray, L. M. & Tout, C. A. 2007, MNRAS, 376, 61  
 Eldridge, J. J. & Stanway, E. R. 2016, MNRAS, 462, 3302  
 Finn, L. S. 1996, Phys. Rev. D, 53, 2878  
 Fryer, C. L., Belczynski, K., Wiktorowicz, G., et al. 2012, ApJ, 749, 91  
 Giacobbo, N. & Mapelli, M. 2018, Monthly Notices of the Royal Astronomical Society, 480, 2011  
 Hunter, J. D. 2007, Computing in Science and Engineering, 9, 90  
 Iglesias, C. A. & Rogers, F. J. 1993, ApJ, 412, 752  
 Iglesias, C. A. & Rogers, F. J. 1996, ApJ, 464, 943  
 Ivanova, N., Justham, S., Chen, X., et al. 2013, A&A Rev., 21, 59  
 Ivanova, N., Justham, S., & Podsiadlowski, P. 2015, Monthly Notices of the Royal Astronomical Society, 447, 2181  
 Ivanova, N. & Taam, R. E. 2004, The Astrophysical Journal, 601, 1058  
 Jones, E., Oliphant, T., Peterson, P., et al. 2001–, SciPy: Open source scientific tools for Python, [Online; accessed <today>]  
 Kippenhahn, R., Ruschenplatt, G., & Thomas, H. C. 1980, A&A, 91, 175  
 Kroupa, P., Tout, C. A., & Gilmore, G. 1993, MNRAS, 262, 545  
 Kruckow, M. U., Tauris, T. M., Langer, N., Kramer, M., & Izzard, R. G. 2018, MNRAS, 481, 1908  
 Kruckow, M. U., Tauris, T. M., Langer, N., et al. 2016, A&A, 596, A58  
 Kudritzki, R.-P. & Puls, J. 2000, ARA&A, 38, 613  
 Langer, N., Fricke, K. J., & Sugimoto, D. 1983, A&A, 126, 207  
 Langer, N. & Norman, C. A. 2006, ApJ, 638, L63  
 Lipunov, V. M., Postnov, K. A., & Prokhorov, M. E. 1997, Astronomy Letters, 23, 492  
 Madau, P. & Fragos, T. 2017, ApJ, 840, 39  
 Marchant, P., Langer, N., Podsiadlowski, P., et al. 2017, A&A, 604, A55  
 Marchant, P., Langer, N., Podsiadlowski, P., Tauris, T. M., & Moriya, T. J. 2016, A&A, 588, A50  
 Nandez, J. L. A., Ivanova, N., & Lombardi, J. C. J. 2015, Monthly Notices of the Royal Astronomical Society, 450, L39  
 Neijssel, C. J., Vigna-Gómez, A., Stevenson, S., et al. 2019, MNRAS, 490, 3740  
 Nugis, T. & Lamers, H. J. G. L. M. 2000, A&A, 360, 227  
 O'Connor, E. & Ott, C. D. 2011, The Astrophysical Journal, 730, 70  
 Packet, W. 1981, A&A, 102, 17  
 Paczynski, B. 1991, ApJ, 370, 597  
 Pavlovskii, K. & Ivanova, N. 2015, MNRAS, 449, 4415  
 Pavlovskii, K., Ivanova, N., Belczynski, K., & Van, K. X. 2017, MNRAS, 465, 2092  
 Paxton, B., Bildsten, L., Dotter, A., et al. 2010, MESA: Modules for Experiments in Stellar Astrophysics  
 Paxton, B., Bildsten, L., Dotter, A., et al. 2011, ApJS, 192, 3  
 Paxton, B., Cantillo, M., Arras, P., et al. 2013, ApJS, 208, 4  
 Paxton, B., Schwab, J., Bauer, E. B., et al. 2018, ApJS, 234, 34  
 Paxton, B., Smolec, R., Schwab, J., et al. 2019, ApJS, 243, 10  
 Perez, F. & Granger, B. E. 2007, Computing in Science and Engineering, 9, 21  
 Peters, P. C. 1964, Physical Review, 136, 1224  
 Podsiadlowski, P. 2001, in Astronomical Society of the Pacific Conference Series, Vol. 229, Evolution of Binary and Multiple Star Systems, ed. P. Podsiadlowski, S. Rappaport, A. R. King, F. D'Antona, & L. Burderi, 239  
 Popham, R. & Narayan, R. 1991, ApJ, 370, 604  
 Quast, M., Langer, N., & Tauris, T. M. 2019, A&A, 628, A19  
 Ritter, H. 1988, A&A, 202, 93  
 Rodriguez, C. L., Chatterjee, S., & Rasio, F. A. 2016, Phys. Rev. D, 93, 084029  
 Sana, H., de Mink, S. E., de Koter, A., et al. 2012, Science, 337, 444  
 Soberman, G. E., Phinney, E. S., & van den Heuvel, E. P. J. 1997, A&A, 327, 620  
 Spera, M., Mapelli, M., Giacobbo, N., et al. 2019, Monthly Notices of the Royal Astronomical Society, 485, 889  
 Stevenson, S., Vigna-Gómez, A., Mandel, I., et al. 2017, Nature Communications, 8, 14906  
 Strolger, L.-G., Riess, A. G., Dahlen, T., et al. 2004, ApJ, 613, 200  
 Sukhbold, T. & Adams, S. 2020, MNRAS, 492, 2578  
 Sukhbold, T., Ertl, T., Woosley, S. E., Brown, J. M., & Janka, H. T. 2016, The Astrophysical Journal, 821, 38  
 Sukhbold, T. & Woosley, S. E. 2014, The Astrophysical Journal, 783, 10  
 Tauris, T. M., Kramer, M., Freire, P. C. C., et al. 2017, ApJ, 846, 170  
 Tauris, T. M. & van den Heuvel, E. P. J. 2006, Formation and evolution of compact stellar X-ray sources, Vol. 39, 623–665  
 Thorne, K. S. & Zytckow, A. N. 1977, ApJ, 212, 832  
 Ugliano, M., Janka, H.-T., Marek, A., & Arcones, A. 2012, The Astrophysical Journal, 757, 69  
 van der Walt, S., Colbert, S. C., & Varoquaux, G. 2011, Computing in Science and Engineering, 13, 22  
 Vink, J. S., de Koter, A., & Lamers, H. J. G. L. M. 2001, A&A, 369, 574  
 Voss, R. & Tauris, T. M. 2003, MNRAS, 342, 1169  
 Webbink, R. F. 1984, ApJ, 277, 355

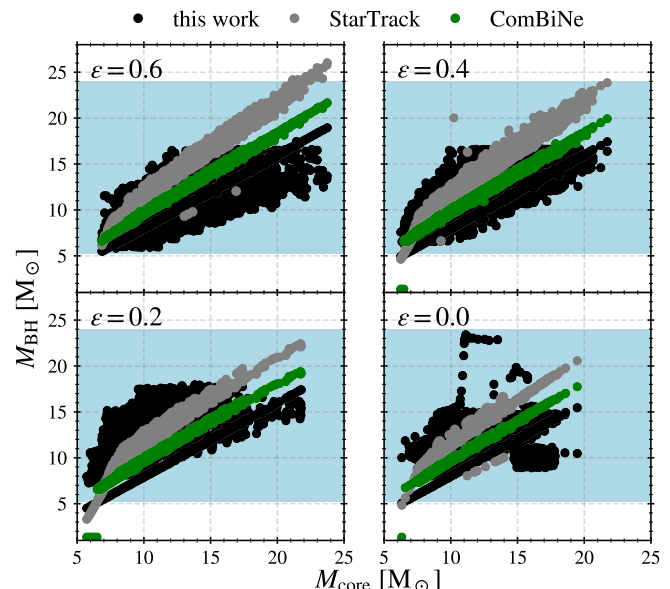


**Fig. A.1.** Masses of black holes formed in all of our BBHs. Different colours represent prescriptions used by other authors. Light blue regions correspond to the range of masses of GW151226 and GW170608. See text for details.

## Appendix A: Black hole formation

Several authors have studied compact object formation using hydrodynamical simulations showing that a fallback of the envelope into the BH is possible. In this work, for simplicity we estimate the mass of the BH produced at the end of the stellar evolution by assuming that it is formed from the collapsed CO-core of a star, specifically,  $M_{\text{BH}} = 0.8 M_{\text{core}}$ . Furthermore, the envelope mass is assumed to be instantly ejected from the binary without interacting with the companion. These sudden mass changes have a direct impact on the orbital dynamics which we solve following Bhattacharya & van den Heuvel (1991):

$$a_{\text{post-SN}} = \frac{\mu}{2\mu - 1} a_{\text{pre-SN}}, \quad e_{\text{post-SN}} = \frac{1 - \mu}{\mu} \quad (\text{A.1})$$

where  $\mu = (M_{\text{post-SN},1} + M_{\text{post-SN},2})/(M_{\text{pre-SN},1} + M_{\text{pre-SN},2})$ . We also check for disruption at BH formation, given by  $e_{\text{post-SN}} > 1$ .

After updating the orbital parameters, a simulation is resumed by evolving a star plus a point mass source in MESAbinary.

In Figure A.1 we compare black holes masses obtained with our prescription of retaining an 80% of the core mass with those from (StarTrack, Belczynski et al. 2008) and (ComBiNe, Kruckow et al. 2018). As shown in this figure, we produce the lightest BHs from the three prescriptions; however, in the range of interest of this work ( $M_{\text{BH}} \sim 5 - 20 M_{\odot}$ ), differences are of just a few solar masses. We also find that in the range of masses we have studied (see Appendix B), our compact objects have masses  $\gtrsim 5 M_{\odot}$ , heavier than any NS, thus we only form BHs, which is in agreement with results from several studies (e.g., O'Connor & Ott 2011; Ugliano et al. 2012; Sukhbold & Woosley 2014; Sukhbold et al. 2016; Sukhbold & Adams 2020).

## Appendix B: MESA runs: full parameter space exploration

As explained in Section 2.5, for this work we explored a wide range of the parameter space defined by the binary initial parameters:  $M_{i,1}$ ,  $M_{i,2}$  and  $a_i$  with the main goal of finding the target regions of solutions that correspond to models compatible with binary progenitors of the GW170608 and GW151226 events. This task was performed for four different values of MT efficiencies and metallicities. For this purpose, we started by the exploration of the target regions corresponding to  $\alpha_{CE} = 2.0$ , which naturally leads to a higher amount of solutions compatible with the GW events with respect to  $\alpha_{CE} = 1.0$ , since the fraction of CE mergers is much lower as the CE is more efficiently removed. For this we used a grid of even numbers for  $M_{i,1}$  and odd numbers for  $M_{i,2}$  ( $\Delta M = 2 M_\odot$ ) and a logarithmic separation in  $a_i$  of 0.02 dex. We first started by simulating progenitor masses giving CO cores leading to BHs compatible with the observed BH masses and later expanding the regions until no compatible solutions were found. Once these target regions were fully covered, we switched to the exploration of the  $\alpha_{CE} = 1.0$  case. For this, since we already counted with the initial exploration, we focused on the binary models that lead to CE triggers, which we re-run using the low CE efficiency. Since these target regions are naturally smaller, we decreased the grid to  $\Delta M = 1 M_\odot$  and 0.01 dex for  $a_i$  to have a better coverage. For each CE survival we also simulated the neighbours in the grid until the target regions were fully covered, in an iterative fashion.

In Figures B.1 and B.2 we present the full parameter space explored using  $\alpha_{CE} = 2.0$  and 1.0, respectively. Panels from top to bottom correspond to each set of MT efficiencies:  $\epsilon = 0.6, 0.4, 0.2$  and 0.0. Panels from left to right correspond to each set of metallicities:  $Z = 0.015, 0.007, 0.004, 0.001$ . Blue (red) circles are used for models compatible with GW170608 (GW151226). The size of the circles is proportional to the initial separation ( $a_i$ ). Orange circles represent models leading to BBHs that merge within the Hubble time but with  $M_{chirp}$  incompatible with the GW events considered. Gray circles are used for the rest of the models used for this work. In Table B.1 and B.2 we summarise the main characteristics of all the runs performed, including total runs, total of runs leading to BBHs, total runs leading to BBHs that merge within the Hubble time, total runs compatible with GW170608 and GW151226 and the ranges covered in the parameter space defined by  $M_{i,1}$ ,  $M_{i,2}$  and  $a_i$  for each MT efficiency ( $\epsilon$ ) and metallicity ( $Z$ ).

## Appendix C: MESA example

In order to illustrate the evolutionary channel explored throughout this work, we present the full evolution of a binary system which ends its evolution as a BBH compatible with one of the events detected by the LVC, using the two values for the CE efficiency ( $\alpha_{CE} = 2.0$  and 1). The initial parameters for the model are:  $M_{i,1} = 35 M_\odot$ ,  $M_{i,2} = 32 M_\odot$ ,  $a_i = 83.05 R_\odot$ ,  $Z = 0.007$ , and a MT efficiency of  $\epsilon = 0.4$ .

In Figure C.1 we present a scheme for the full binary evolution channel followed by the system from ZAMS to the BBH merger. In general, once the primary (most massive) star expands, the system experiences an initial stable MT phase until the primary contracts and later collapses to form a first BH. Later on, once the secondary expands, a new phase of stable MT develops and the system becomes an X-ray binary. If the MT becomes unstable, a short CE phase is triggered, and the binary separation is heavily reduced while the donor envelope is removed. After

separation, a second BH is formed leading to a BBH that will eventually coalesce through the emission of GWs.

In Figure C.2 we present the full binary evolution Hertzsprung-Russell (HR) diagram corresponding to the example binary systems. In this HR diagram, the primary and secondary stars are born in the ZAMS (in the bottom right part of the figure) and end forming BHs (in the upper left part of the plot). After the primary star expands, two stable MT phases develop: the so-called cases AB and B indicated in light-blue and green, respectively. The luminosity of the primary increases until separation occurs. Then, the primary contracts, moving to the left forming a Wolf-Rayet star. Later on, it collapses to a BH (black star in the figure). Meanwhile, the secondary continues its evolution. After leaving the MS, the secondary expands and a stable MT phase commences (Case AB to BH indicated with salmon colour). This continues until an unstable CE phase is triggered (at the grey circle). A fast out-of-equilibrium phase is developed until separation of the secondary occurs at the blue and orange circles, for  $\alpha_{CE} = 2.0$  and 1 respectively. The secondary evolution then continues until a second BH is formed.

During the short ( $\gtrsim 100$  yr) unstable CE phase, the binary system evolves quickly as the orbital energy is extracted to unbind the envelope of the donor. In Figure C.3 we show the evolution of the binary parameters during the CE phase for both CE efficiencies. In the top panel we show the evolution of the donor mass loss ( $\dot{M}_{RLOF}$ ), in the mid panel the binary separation ( $a$ ) and in the bottom panel the relative overflow defined as  $f(R, R_{RL}) = (R - R_{RL})/R_{RL}$ . Furthermore, in Figure C.4 we focus on the evolution of the donor parameters. From top to bottom we present the donor radius, total mass, superficial H mass fraction and relative overflow.

Once the CE is triggered ( $\tau_{CE} = 0$ ), the donor mass loss grows linearly for 10 yr from stable MT value to the fixed rate of  $10^{-1} M_\odot \text{ yr}^{-1}$ . During the early phase, the binary separation shrinks faster than the donor radius and thus the relative overflow increases, until this effect is reversed at 50–60 yr. After that, the donor star shrinks faster until separation is reached at  $\sim 80$  yr, after the beginning of the CE phase. At this point the mass loss rate decreases until the thermal scale is recovered ( $\dot{M}_{RLOF} \approx \dot{M}_{th}$ ) and the CE phase is finished. As a result of the CE phase, the envelope of the donor star is removed. In particular, in the  $\alpha_{CE} = 1.0$  case, no H is left, while in the  $\alpha_{CE} = 2.0$  case a small fraction of H remains, but its total mass decreases by  $\sim 7 M_\odot$ . In both cases, a strong decrease of a factor of  $\sim 10$  in the orbital separation is seen, leading to an ultra-compact binary which eventually will become a BBH that will merge within the Hubble time.

## Appendix D: Merger time delay calculation

In a binary consisting of two BHs, orbital shrinking is driven by the emission of gravitation waves, which ends up with a merger of the BHs. In order to estimate the time needed for a BBH to merge after its formation, which is also known as merger time delay, we use the prescription given by Peters (1964):

$$t_{\text{merger}} = \frac{15}{304} \frac{a_0^4 c^5}{G^3 m_1 m_2 (m_1 + m_2)} \times \left[ \left(1 + e_0^2\right) e_0^{-12/19} \left(1 + \frac{121}{304} e_0^2\right)^{-870/2299} \right]^4 \times \int_0^{e_0} de \frac{e^{29/19} [1 + (121/304) e^2]^{1181/2299}}{(1 - e^2)^{3/2}} \quad (\text{D.1})$$

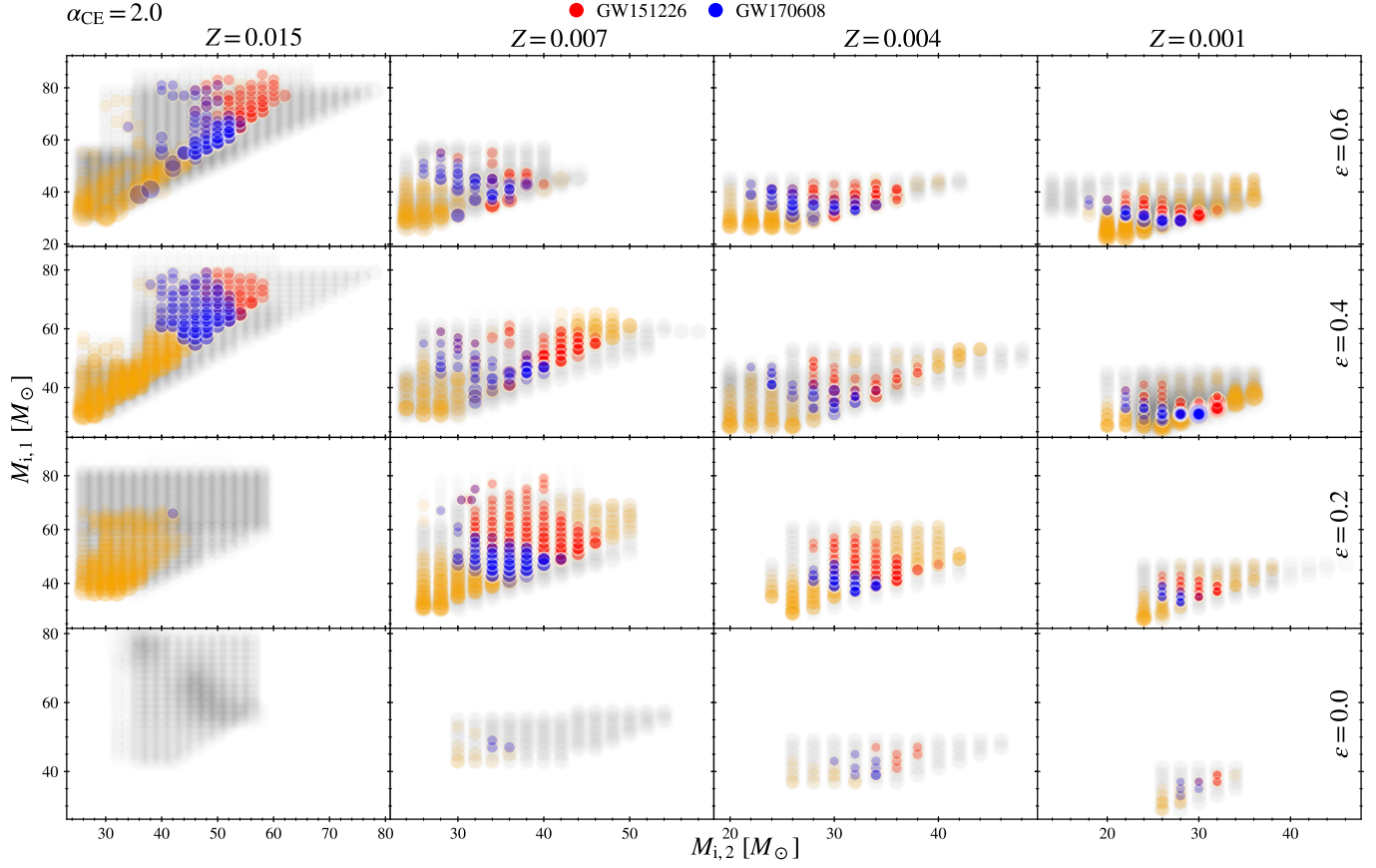


**Fig. B.1.** Full parameter space explored using  $\alpha_{\text{CE}} = 2.0$ . See text for details.

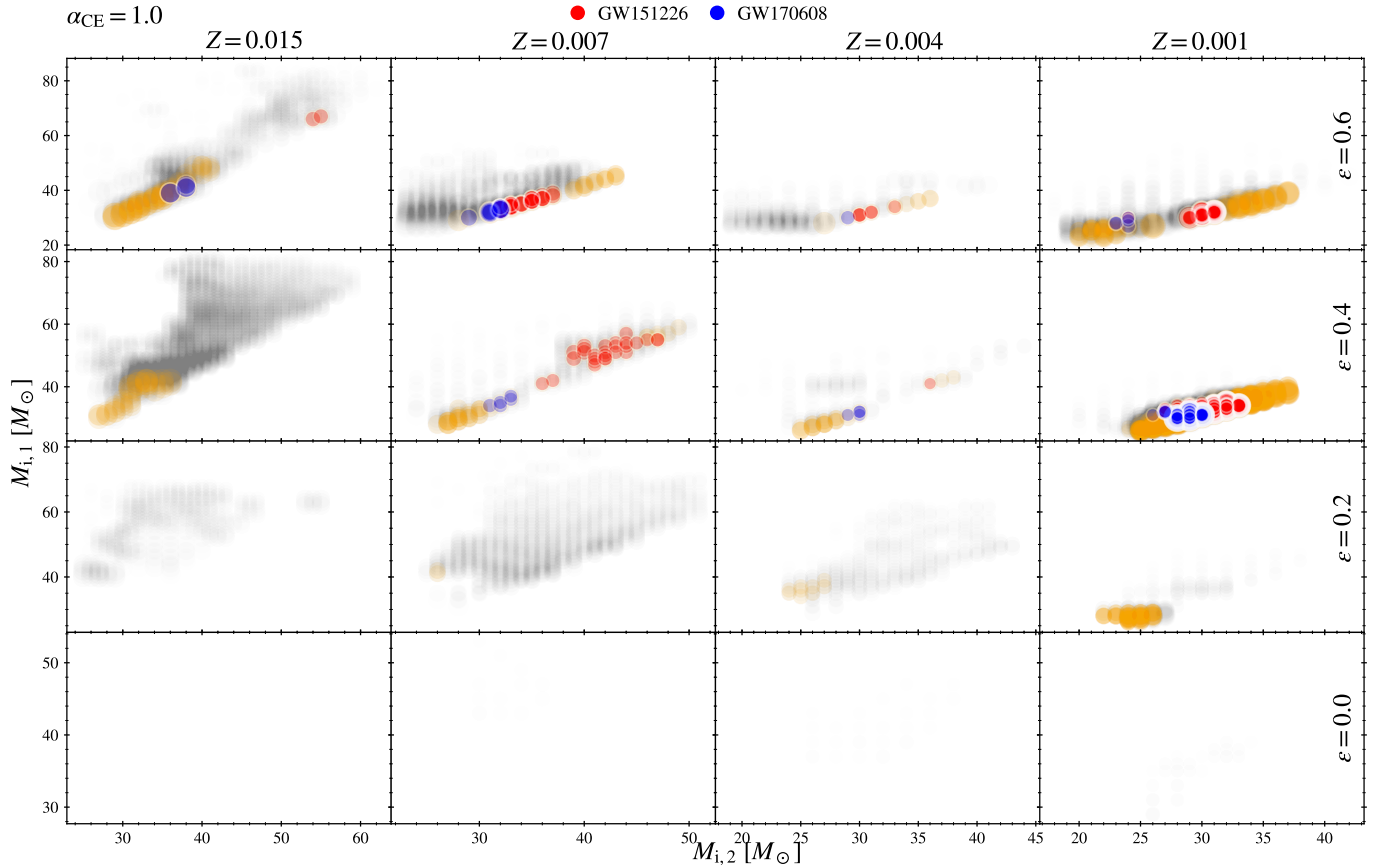


**Fig. B.2.** Idem to Figure B.1 for  $\alpha_{\text{CE}} = 1.0$ .

**Table B.1.** Summary of MESA runs performed with  $\alpha_{\text{CE}} = 2.0$ .

$\epsilon$	$Z$	Runs	BBH	BBH ( $< t_{\text{Hubble}}$ )	GW170608	GW151226	$M_{i,1} [\text{M}_\odot]$	$M_{i,2} [\text{M}_\odot]$	$a_i [\text{R}_\odot]$
0.6	0.001	1637	1042	261	31	48	23–45	14–36	36–300
	0.004	1160	743	191	46	51	27–45	20–42	36–150
	0.007	1820	1070	159	45	22	27–57	24–44	36–200
	0.015	5207	2617	288	80	70	31–89	26–78	36–200
0.4	0.001	1532	1253	232	42	47	27–45	20–36	30–500
	0.004	2187	1403	205	33	41	27–53	20–48	36–200
	0.007	2424	1382	266	53	71	31–65	24–58	36–200
	0.015	3458	1621	450	114	51	31–85	26–78	52–200
0.2	0.001	986	620	123	16	30	27–47	24–46	30–100
	0.004	1202	750	251	41	66	29–61	24–42	36–91
	0.007	2741	1496	430	89	138	31–83	26–50	36–150
	0.015	4962	3077	318	1	0	37–91	26–58	36–150
0.0	0.001	348	324	25	5	5	29–41	26–34	36–100
	0.004	744	592	28	8	6	37–49	26–46	36–100
	0.007	1102	766	13	3	0	43–57	30–54	36–150
	0.015	2135	1876	0	0	0	43–79	32–56	30–2000

**Table B.2.** Summary of MESA runs performed with  $\alpha_{\text{CE}} = 1.0$ .

$\epsilon$	$Z$	Runs	BBH	BBH ( $< t_{\text{Hubble}}$ )	GW170608	GW151226	$M_{i,1} [\text{M}_\odot]$	$M_{i,2} [\text{M}_\odot]$	$a_i [\text{R}_\odot]$
0.6	0.001	2043	1095	179	5	57	22–55	18–42	36–315
	0.004	736	186	14	1	6	27–45	19–41	36–174
	0.007	2084	994	65	12	36	27–55	23–43	43–180
	0.015	1637	768	75	5	2	30–85	26–62	43–220
0.4	0.001	2454	2093	986	205	337	26–45	20–37	33–314
	0.004	422	211	30	4	1	26–53	20–44	40–105
	0.007	1107	469	71	5	27	28–65	24–50	40–150
	0.015	4713	1511	39	0	0	30–81	25–59	52–210
0.2	0.001	482	328	95	0	0	26–47	22–38	36–141
	0.004	844	295	9	0	0	29–62	24–43	43–83
	0.007	2255	620	2	0	0	31–79	25–51	43–122
	0.015	852	328	0	0	0	40–68	25–55	43–142
0.0	0.001	50	2	0	0	0	29–39	26–34	36–63
	0.004	28	1	0	0	0	37–47	26–38	40–57
	0.007	13	1	0	0	0	43–53	30–36	43–63
	0.015	–	–	–	–	–	–	–	–

where  $a_0$  and  $e_0$  are the semi-major axis and eccentricity at BBH formation, while  $m_1$  and  $m_2$  are BH masses.

at BBH formation: increasing it in only one order of magnitude increases  $t_{\text{merger}}$  by a factor  $10^4$ .

## Appendix E: Dependence of the merger rates on the star formation history

Neijssel et al. (2019) show that the uncertainties in the metallicity evolution and star formation history can change the rates of BBH mergers. Thus, we perform the evaluation of detectable rates during O1/O2 observing runs for the progenitor population of the GW151226 and GW170608 for different SFRs and metallicity distributions. For the SFRs and in addition to the already mentioned SFR from Strolger et al. (2004), we use the SFR from Madau & Fragos (2017). For the evolution of metallicity over cosmic time, we compare Langer & Norman (2006) distribution with the fiducial model of Neijssel et al. (2019).

In Figure E.1 we present merger rates for different combinations of star formation evolution over cosmic time. Our results show that the strongest changes in event rates are introduced by the metallicity distribution, while the different SFRs assumed produce less variations in the outcome rates. These results are similar to the ones found by Chruslinska & Nelemans (2019)

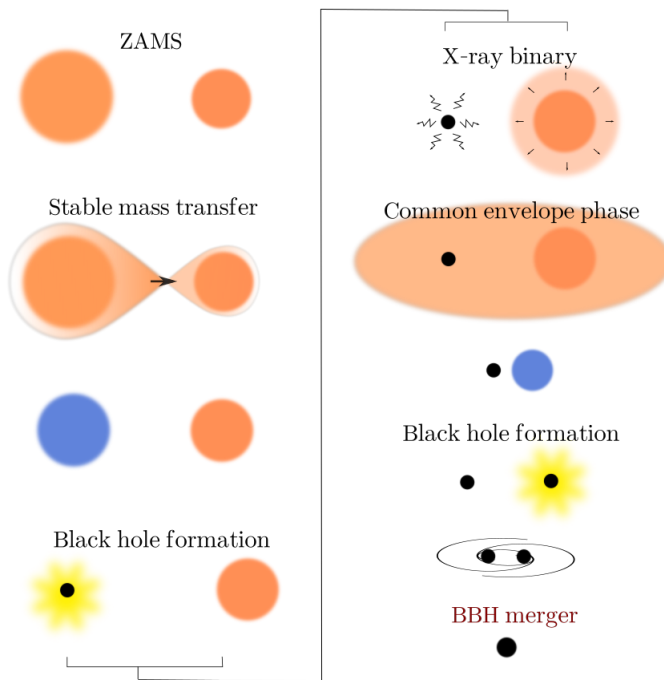


**Fig. C.1.** Schematic view of the binary evolutionary channel explored throughout this work.

and Neijssel et al. (2019). For some cases, we find differences in the rates of more than a factor of two. In all cases, the maximum value for the detection rate remains lower than  $0.5 \text{ yr}^{-1}$ .

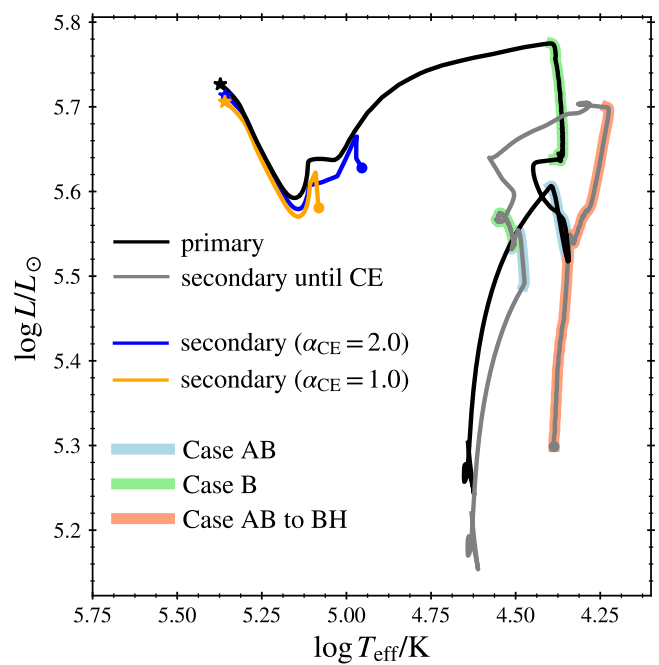


**Fig. C.2.** Full binary evolution HR diagram of the binary system considered in the example. Primary and secondary stars are born in the ZAMS (bottom right). Case AB (B) stable MT phase is indicated in light-blue (green). After them the primary moves to the left and collapses to form a first BH (black star). The secondary expands and a Case AB stable MT phase occurs (salmon colour) until an unstable CE phase is triggered (grey circle). The detach of the secondary occurs at the blue (orange) circle for  $\alpha_{\text{CE}} = 2.0$  ( $\alpha_{\text{CE}} = 1.0$ ). A second BH is formed at the top left corner (coloured stars).

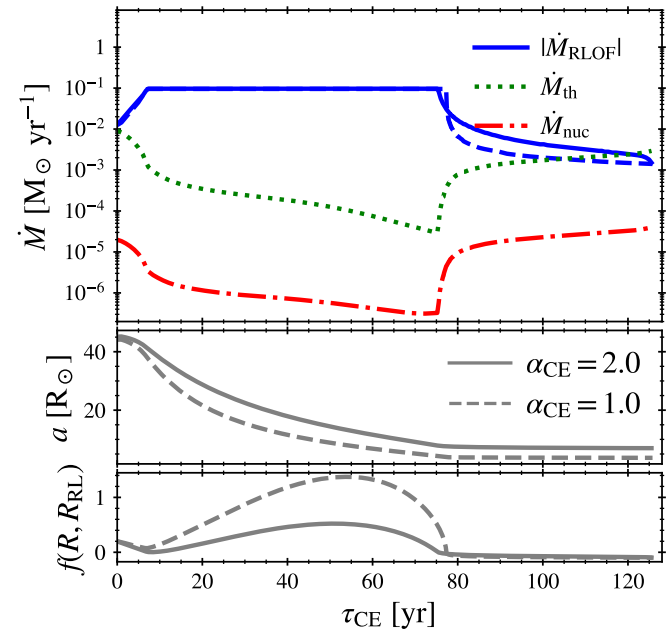


**Fig. C.3.** Evolution of binary parameters across the CE phase. On the top panel we present the evolution of the donor mass loss ( $\dot{M}_{\text{RLOF}}$ , blue) and mass transfer scales: thermal ( $\dot{M}_{\text{th}}$ , dotted green) and nuclear ( $\dot{M}_{\text{nuc}}$ , dot-dashed red). On the mid panel, the separation ( $a$ ) and on the lower panel the relative overflow ( $f(R, R_{\text{RL}})$ ). Solid (dashed) lines represent  $\alpha_{\text{CE}} = 2.0$  ( $\alpha_{\text{CE}} = 1.0$ ).

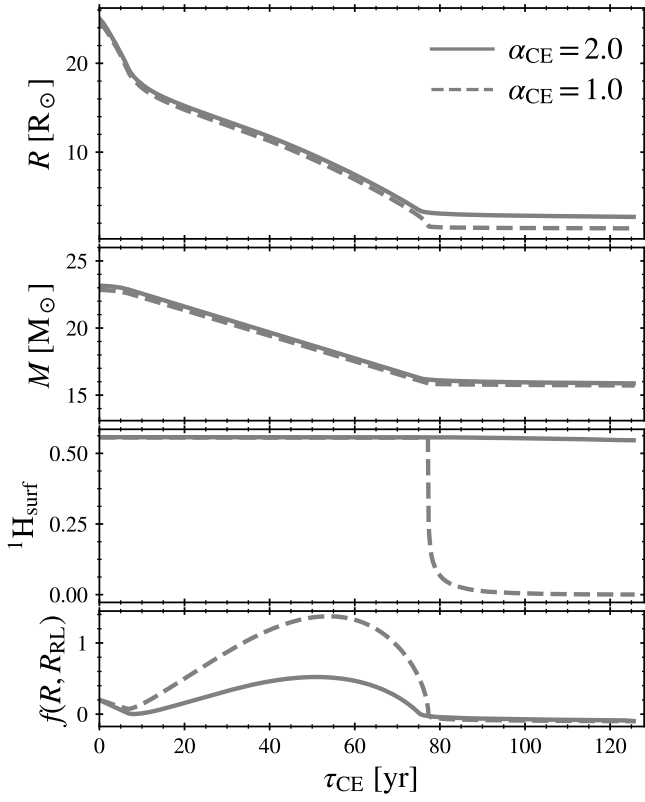


**Fig. C.4.** Evolution of donor star parameters during the CE phase. From top to bottom we present the evolution of the donor radius ( $R$ ), donor total mass ( $M$ ), superficial H mass fraction, and the relative overflow ( $f(R, R_{\text{RL}})$ ). Solid (dashed) lines represent  $\alpha_{\text{CE}} = 2.0$  ( $\alpha_{\text{CE}} = 1.0$ ).

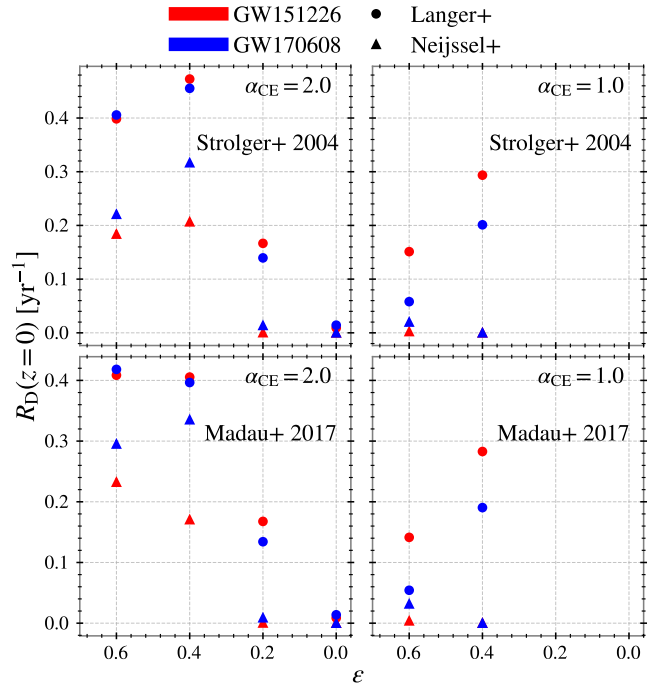


**Fig. E.1.** Total detection rates for O1 and O2 runs,  $R_D(z = 0)$ , marginalised over metallicity, as a function of MT efficiency  $\epsilon$  for  $\alpha_{\text{CE}} = 2.0$  (left panel) and  $\alpha_{\text{CE}} = 1.0$  (right panel) of events compatible with GW151226 (red) and GW170608 (blue) within their 100% credible intervals. Circles represent detection rates assuming the metallicity evolution given in Langer & Norman (2006) while triangles are the rates using the metallicity distribution of Neijssel et al. (2019).

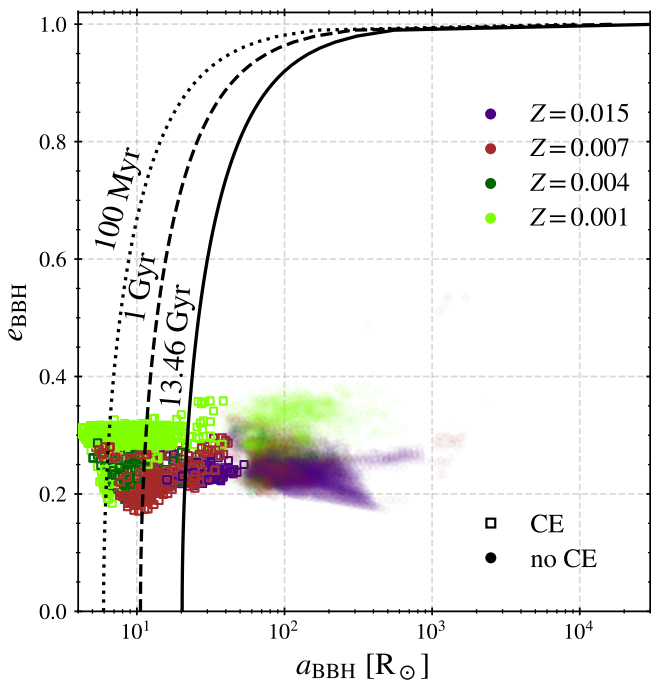


**Fig. D.1.** Final binary parameters for all our BBHs with  $M_{\text{chirp}}$  consistent with GW151226 and/or GW170608. Colours indicate different metallicities (see legend). Dotted, dashed and solid black lines correspond to values of constant  $t_{\text{merger}}$ : 100 Myr, 1 Gyr,  $\tau_{\text{Hubble}}$ , respectively, assuming BHs masses of 12.3 and 7.65  $M_{\odot}$ .